Modelling Magnetic Phase Transitions

with Density Functional Theory and the Finite Element Method

Mischa van Diepen

Modelling Magnetic Phase Transitions with Density Functional Theory and the Finite Element Method

Faculty of Applied Sciences
Department Radiation, Science & Technology
Fundamental Aspects of Materials and Energy (FAME)

Faculty of Electric Engineering, Mathematics & Computer Science
Department of Applied Mathematics
Numerical Analysis

June 2019
Bachelor's Thesis Applied Physics & Applied Mathematics
Delft University of Technology

By:

Mischa van Diepen

Supervised by:
Dr. ir. N. van Dijk
Dr. ir. F. Vermolen
I. Batashev

Summary

The present thesis discusses two modelling endeavours that serve to provide insights into both the magnetic and structural dynamics associated with a first order magnetic phase transition.

Firstly, density functional theory has been used to model the lithiation of a supercell of $2\times2\times2$ the conventional unit cell of the ferromagnet Fe_2P. Subsequently, the magnetic moments in the resulting structure were set to proxy a paramagnetic state and compute the energy difference between the ferromagnetic and paramagnetic state. It has been found that non-magnetic Li-atoms substitute for magnetic Fe-atoms at $3g$-positions in the the a,b-plane. Moreover, since these are the positions of Fe-atoms that carry a high magnetic moment and induce a magnetic moment on the Fe-atoms in the $3f$-layer, the lithiation of the respective positions leads to a reduction of the magnetic moment per formula unit. The energy difference between the ferromagnetic state and the selected proxy of a paramagnetic state showed to decrease linearly in the fraction of lithiated $3g$-positions. This deviates from experimental findings suggesting an increase of T_C of the structure upon lithiation. This difference can stem from the fact that the lithiation fractions considered here were higher than those achieved experimentally or that the selected proxy of a paramagnetic state was incorrect.

Secondly, the finite element method has been applied to approximate the displacement field of a 2D structure consisting of grains distributed over two structural phases with different associated lattice parameters. The development of shear stress discontinuities across grain boundaries has been studied in relation to the degree of porosity in a domain. The replacement of grain boundaries by voids appears, after correction for the orientation of edges at these grain boundaries, to lead to a reduction in the values for these discontinuities. More delicate development of the grid to correspond to physically realistic orientations of grain boundaries is needed to gain more robust quantitative measures for this relation. Moreover, the relation between the orientation of grain boundaries and shearing stresses at these boundaries forms an interesting venue for further research to which the present FEM-model can be readily applied.

List of abbreviations

Acronyms		Mathematical symbols & Physical quantities	
DFT	Density Functional Theory	$\mathbf{a}$, $\mathbf{b}$, $\mathbf{c}$	Lattice vectors
FEM	Finite Element Method	A	Element area
FOMT	First Order Magnetic Phase Transition	$\mathbf{B}$	Interpolation matrix of strain
GMCE	Giant Magnetocaloric Effect	C	Heat capacity
MCE	Magnetocaloric Effect	$\mathbf{d}$	Nodal displacement vector
SOMT	Second Order Matnetic Phase Transition	$\mathbf{D}$	Elasticity matrix
VASP	Vienna Ab Initio Simulation Package	E	Young's modulus
		$\mathbf{H}$	Magnetic field
		J	Exchange interaction coefficient
		$\mathbf{M}$	Magnetization
		$\mathbf{N}$	Interpolation matrix of displacement
		S	Entropy
		T_C	Curie temperature
		ΔT_{ad}	Adiabatic temperature change
		$\mathbf{u}(\mathbf{x})$	Displacement field

Greek letters	
α_x, α_y	Expansion coefficients
$\boldsymbol{\mu}$	Magnetic moment
ν	Poisson's ratio
$\boldsymbol{\varepsilon}$	Strain tensor
Π	Potential energy
$\boldsymbol{\sigma}$	Stress tensor
$\sigma_{xx}, \sigma_{yy}, \tau_{xy}$	Stress tensor components
$[\![\tau]\!]$	Shear stress discontinuity across edge
ϕ	Phase indicator

Contents

1 Introduction

A promising field of research within the subject of materials sciences revolves around the magnetocaloric effect (MCE). In this phenomenon the application of an external magnetic field to a material with magnetic degrees of freedom leads to a temperature increase of the respective material [1] [2]. Accordingly, energy transfers from magnetic states to energy stored in temperature differences, and vice versa. A promising application of the MCE is magnetic refrigeration [3]. Here, the cyclic application of an external magnetic field to a material and the consequent removal of heat due to a temperature difference with the environment leads to a process with, firstly, a higher efficiency than conventional, compression gas-based refrigeration techniques and, secondly, depletion of the ozone layer due the use of harmful gases does not occur [3] [4]. Another possible application of the MCE rests in the cyclic magnetization and demagnetization of a material as the temperature of its local environment is changed. Accordingly, the waste heat of some industrial process can be exploited to generate rotational motion [5].

In the search for magnetocaloric materials with optimal characteristics for the above processes, several factors are of importance. Firstly, the magnitude of the MCE, the temperature change over a unit of magnetic field change, is desired to be big [6]. Secondly, the temperature range in which this effect is greatest should coincide with the desired temperature range in which the process is expected to operate [3]. For example, the operational temperature of refrigerating cycles lays near room temperature. Lastly, changes in the lattice parameters of a magnetocaloric material during the MCE should be limited or mitigated as to prevent the progressive development of fractures in the material due to the buildup of shear and tensile stresses [6].

The present thesis addresses two of these aspects and is correspondingly divided into two parts. Firstly, using Density Functional Theory (DFT), the process of lithiation of Fe_2P is modelled. Fe_2P is a ferromagnetic material with a Curie Temperature (T_C) of around 217 K [7] [8]. Experimentally it was discovered that the substitution of nonmagnetic Li-atoms for magnetic Fe-atoms in this material leads to a significant increase of this T_C [9]. Using DFT, it is the objective to find the preferred position for Li-atoms in this lattice and thereupon to estimate the structure's transition temperature and its dependence on the lithium content.

Secondly, a mathematical model is developed to account for the buildup of stresses in a material during a magnetic phase transition. Here, the Finite Element Method (FEM) is applied to approximate the minimum energy state of a 2D material in which domains are randomly distributed over two phases and correspondingly have different equilibrium dimensions. This model is then manipulated to allow for the introduction of porosity into the bulk of the material. Finally, it is the objective to find a relation between the shear stress and the degree of porosity in such a material.

The outline of the present thesis is as follows. Firstly, in chapter 2, the general physical background of the MCE is considered, as well as the determinants of the T_C of a material and some experimental findings relating to fracturing during magnetic phase transitions. Subsequently, we move to the first part of this work related to the modelling of the lithiation of Fe_2P through DFT. Here, chapter 3 deals with the fundamental aspects of DFT and the methodology, whereas chapter 4 provides the results and a discussion. The second part part is dedicated to the development of an FEM-model of the development of internal forces during a magnetic phase transition. Chapter 5 introduces the FEM and its application to continuum mechanics while it leads the reader through the development of a model. Chapter 6 presents the respective results. Chapter 7 provides a combined conclusion to both parts of this thesis.

2 Theory

In the present chapter, the magnetocaloric effect (MCE) is introduced. Moreover, the chapter briefly discusses literature relating to the two topics that are subject to the modelling endeavors in this thesis, namely the tuning of the working temperature of a magnetocaloric material and the buildup of internal stresses during a magnetic phase transition.

2.1 The magnetocaloric effect

An intuitive description of the magnetocaloric effect can be given on the basis of thermodynamic variables, thus disregarding the actual mechanics of the phenomenon at an atomic level [1][10]. Firstly, we assume to be operating under adiabatic conditions, thus holding the total entropy of a system under consideration constant. In the absence of an external magnetic field the magnetic moments of a material in a paramagnetic state will be randomly oriented, translating into a high magnetic entropy. When the material is placed in an external magnetic field, the moments will generally align to the magnetic field. Since this leads to a reduction of the magnetic entropy, the randomness of the orientation of the magnetic moments, the adiabatic requirement implies that an increase in the entropy stored in the temperature of the material occurs. In other words, a temperature increase of the material is observed.

This process is now elucidated at the hand of thermodynamic equations [10]. Here, we assume to operate under constant pressure and under adiabatic conditions, thus keeping entropy S constant.

If the magnetization M and entropy S are continuous functions of H and T, the infinitesimal magnetic entropy change is related to the derivative of M with respect tot T at a fixed magnetic field as follows.

$$\Big(\frac{\partial S_M(T,H)}{\partial H}\Big)_T = \Big(\frac{\partial M(T,H)}{\partial T}\Big)_H \tag{1}$$

Now, we use the defining equation of the heat capacity at constant pressure, dependent on H and T.

$$\Big(\frac{\partial S(T,H)}{\partial T}\Big)_H = \Big(\frac{C_P(T,H)}{T}\Big)_H \tag{2}$$

and, expanding dS through the relevant partial derivatives

$$TdS = T\Big(\frac{\partial S(T,H)}{\partial T}\Big)_H dT + T\Big(\frac{\partial S(T,H)}{\partial H}\Big)_T dH \tag{3}$$

Since we assume to operate under adiabatic conditions, TdS in equation 3 equals zero. Accordingly, the infinitesimal adiabatic temperature change due to a change of the magnetic field follows as

$$dT(T,H) = -\Big(\frac{T}{C(T,H)}\Big)_H \Big(\frac{\partial M(T,H)}{\partial T}\Big)_H dH \tag{4}$$

Integration over the magnetic field from H_1 to H_2 yields

$$\Delta T_{ad}(T)_{\Delta H} = \int_{H_1}^{H_2} dT(T,H) = -\int_{H_1}^{H_2} \Big(\frac{T}{C(T,H)}\Big)_H \Big(\frac{\partial M(T,H)}{\partial T}\Big)_H dH \tag{5}$$

The MCE occurs in any material with magnetic degrees of freedom [1]. However, from the expression for ΔT_{ad} in equation 5, it is evident that the temperature change due to a magnetic

field change ΔH depends on the material that is used and the temperature range in which one operates. For a given material, ΔT_{ad} is generally largest at temperatures where the materials magnetic ordering changes quickly with temperature, around a so-called *critical temperature*. In ferromagnetic materials, this critical temperature is the Curie Temperature (T_C). This is the temperature above which the parallel ordering of the magnetic moments in a ferromagnetic material has fully broken into a random order, called paramagnetic.

Here we can differentiate between first order and second order magnetic phase transitions (FOMT and SOMT, respectively). FOMT-materials have a discontinuous first derivative of the magnetization and Gibbs free energy with respect to the temperature, whereas for SOMT-materials this applies to the second derivative of the respective quantities [10]. This implies that the MCE for FOMT-materials is generally stronger than for SOMT-materials. Moreover, in most FOMT-materials, the discontinuous magnetic phase transition goes together with a discontinuous change in the lattice parameters and/or relative atomic positions, leading to so-called magnetostructural phase transitions [3] [6].

Some FOMT-materials exhibit an exceptionally large MCE, leading to the classification of the Giant Magnetocaloric Effect (GMCE). This is generally proposed to be the consequence of the coincidence of the jump in the magnetization of FOMT-materials and the crystal structure, upon which the entropy related to the crystal structure changes as well. leading to so-called magneto-structural effects [3] [6]. During the magnetic phase transition of these materials. For materials exhibiting the GMCE, the associated change in the structural entropy is of the same sign as the change of magnetic entropy[11]. Accordingly, the overall entropy decrease in these materials is unusually high, leading to a higher temperature increase required to keep total entropy constant.

2.2 Tuning the working temperature

In the search for materials possessing magnetocaloric properties suited for applications in for example magnetic refrigeration, not only the size of the magnetocaloric effect is of importance, but also the temperature at which the maximum magnitude of this effect is reached, the critical temperature. For ferromagnetic materials, this is the T_C. This working temperature, which is a material-specific property, is ought to lay around room temperature for purposes of magnetic refrigeration and in the range 20 to 80 °C for the conversion of waste heat into electric energy. An often-quoted ferromagnet possessing favorable magnetocaloric properties is Gadolinium (Gd), a rare earth metal [4]. This metal has a T_C of around 20 °C [12]. The associated material $Gd_5Si_2Ge_2$ exhibits a GMCE of about 50% higher than that observed in Gd [13]. However, since Gd is a rare earth metal, any magnetic refrigeration technique relying on the use of materials containing significant fractions of Gd would be rendered too expensive. Thus, the search is for magnetocaloric materials with comparable properties, but consisting of more readily available materials.

The T_C of a ferromagnetic material logically scales with the (thermal) energy required to break the parallel ordering of the magnetic moments in the respective material [1]. This energy is a function of the number of magnetic positions in the crystal, the magnitude of the magnetic moments at these positions, and the strength of the exchange interaction between the atoms at different positions [14]. For a simple structure with one magnetic atom per unit cell, mean-field approximations result in the following expression for T_C. Here, $J_0 = \sum_j J_{0j}$ is the summation over all exchange interaction coefficients with the magnetic atom in a unit cell and $\mu = \|\boldsymbol{\mu}\|$ the magnetic moment of the respective atom.

$$T_C = \frac{2(\mu + 1)J_0}{3\mu} \tag{6}$$

For structures with more than one symmetrically unique atomic position, this mean field theory approach can be expanded by considering the various sublattices present in the respective lattice [14]. Here, T_C follows as the largest eigenvalue of a system of equations given by equation 7. In this system, $\theta_{mn} = \frac{2}{3k_B} J_0^{mn}$ sums the interaction coefficients of a symmetrically unique atomic position in sublattice m with all positions in sublattice n and S is a vector containing the moments of the symmetrically unique atoms in the respective sublattices.

$$(\mathbf{\Theta} - T\mathrm{I})\mathrm{S} = \mathbf{0} \tag{7}$$

Whereas this mean field estimation of T_C is expected to deviate from the true experimental value upon increasing numbers of sublattices, the qualitative insights into the development of T_C provided by this approximation can be valuable.

Exchange interactions between atoms are highly sensitive to the local environment of the respective atoms and the distance between these atoms. Accordingly, introducing foreign elements into a lattice can not only effect the T_C through the magnetic moments they carry, but also through the influence they have on the crystal structure of the material. It can thus be that, upon the substitution of nonmagnetic elements for magnetic elements, such as Li-atoms for Fe-atoms in Fe_2P [9], one observes an *increase* of the T_C of the material.

To find materials with favorable magnetic properties, it is not always necessary to compose materials and experimentally find the respective working temperature. For example, modelling algorithms such as density functional theory (DFT) enable researchers to draw expectations on the unit cell build up and respective magnetic behavior of alloys subject to investigation. In DFT, the energy-minimizing solution for the Schrödinger equation corresponding to a given system is approximated by fixing the atomic positions and considering the electronic density as a dependent variable. For more detail on DFT, the reader is referred to section 3.1. This so-called ab initio modelling forms a good starting point into the magic land of the magnetocaloric effect and will be used in this report to model the magnetic properties of lithiated Fe_2P.

2.3 Fracture-formation in magnetocaloric materials

As has been discussed above, one of the main characteristics of FOMT-materials is the fact that the magnetocaloric effect occurs simultaneously with a discontinuous change in the lattice parameters and/or the relative atomic positions [6] [11]. Since projected applications of the magnetocaloric effect rest in a cyclic passing of the material through the magnetic phase transition, it is of importance to consider the effect of a repeated passing through such magneto-structural changes on the used materials.

The changes in lattice parameters occurring during a FOMT are considerable. For example, a 2.2% volume change is reported for the phase transition of MnAs [15]. In Fe_2P, the material that is at the core of the first part of this thesis, the discontinuous changes in the lattice parameters a and c upon its FOMT from a ferromagnetic to a paramagnetic state are respectively -0.06% and +0.08% [16]. When a discontinuous change of the lattice parameters is observed between the ferromagnetic and paramagnetic state, the development of stresses in the lattice at interfaces between the two phases is expected. This in turn can lead to fractures in the material. Although in essence, small fractures are not detrimental to the functioning of a material, the propagation of fractures in a material can severely limit its usability. According to Belyea et al., a big disadvantage of the use of FOMT-materials is the fact that due to the repeated passing through magneto-structural changes these materials are subject to "cracking and fatigue, which severely limits their useful lifetime" [17, p. 1].

Moreover, the size of the magnetocaloric effect is reported to change when a material passes through a magnetostructural transition repeatedly, arguably due to the formation of novel cracks

[18]. Likewise, Waske et al. report that the "size and shape of hysteris changes, which is attributed to the opening of cracks, due to strain exerted on the material during the magnetocaloric transition" [18, p. 136]. This explanation comes on top of the so-called virgin effect, the difference in behavior, most notably the value of T_C, of a material the first time it experiences a phase transition and later runs. This effect has been reported for Fe_2P as well [19].

None of these observations lead to the rejection of FOMT-materials as unfit for practical applications, but the above points of critique do require a solution if FOMT-materials are to be applied to cyclic processes such as magnetic refrigerating. In recognition of this fact, Lyubina et al. introduced 20% porosity into a sample of LaFeSi [20]. Although this decreases the optimal, first run energy density of the material, the authors report that "LaFeSi refrigerants with porous architecture do not degrade mechanically during cycling, thus maintaining excellent cooling performance" [20, p. 3735]. This is attributed to the partial removal of grain boundaries, thus reducing the number of phase interfaces at which stresses build up.

Since the introduction of porosity reduces the energy density of a material, it is relevant to study the relation between the percentages and loci of porosity on one hand and the buildup of internal stresses on the other hand. This will be done in the second part of the present thesis.

2.4 Fe_2P

The starting material for the DFT-calculations presented in this thesis is Fe_2P. To facilitate discussion later on in this work, some relevant references relating to this material are discussed here.

Fe_2P is a ferromagnetic material with a T_C of 217 K [7]. Its magnetic phase transition is reported to be of the first order. Its crystal structure is in the hexagonal space group 189 ($P\bar{6}2m$), as presented in figure 1. In this structure, we identify a unit cell with **c** of length 3.458 Å perpendicular to **a** and **b**, and an angle of 120° between **a** and **b**, which have a length of 5.813 Å. Due to the set of transformations (rotation, inversion, and translation) under which this structure is symmetric, we identify two crystallographically unique Fe-positions and two unique P-positions. The positions occupied by the P-atoms are referred to as $1b$ and $2c$, whereas the Fe-atoms occupy $3f$- and $3g$-positions, as presented in table 1 [21]. Given these positions, the lattice parameters, and the values of variables with a degree of freedom, the crystal structure can be constructed.

Table 1: Wyckoff positions of the atoms in Fe_2P [21]. For the Fe-atoms, the respective experimental value of x as presented in [22]. The lengths of the lattice vectors are a = 5.868 Å anc c = 3.458 Å.

Atom	Wyckoff Position	Coordinates	x (Exp.)
Fe	$3f$	(x,0,0), (0,x,0), (-x,-x,0)	0.257
Fe	$3g$	(x,0,$\frac{1}{2}$), (0,x,$\frac{1}{2}$), (-x,-x,$\frac{1}{2}$)	0.595
P	$2c$	($\frac{1}{3}$, $\frac{2}{3}$, 0), ($\frac{2}{3}$, $\frac{1}{3}$, 0)	-
P	$1b$	(0,0,$\frac{1}{2}$)	-

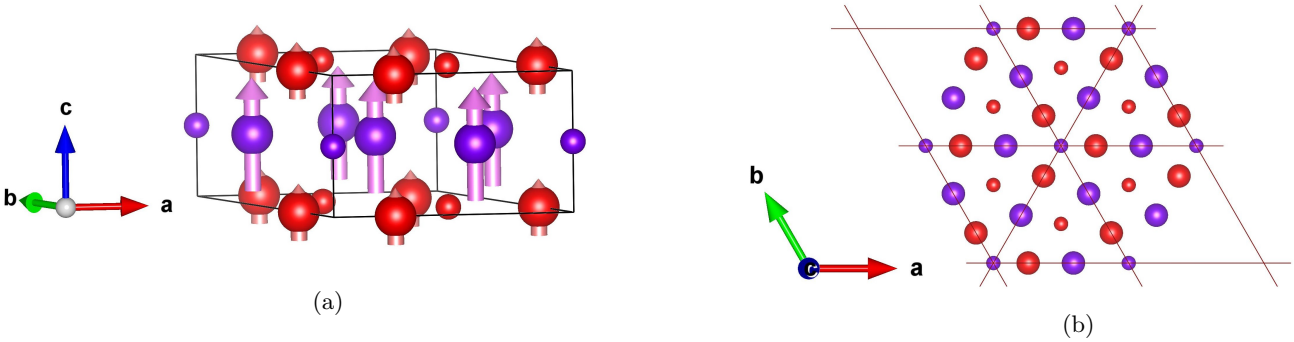

(a) (b)

Figure 1: A unit cell of Fe_2P with magnetic moments in (a) and a view along the c-axis in (b). The $3f$- and $3g$-positions of Fe are indicated by respectively big red and purple spheres, the $2c$- and $1b$-positions of P by small red spheres. The small induced magnetic moments on the P-atoms are not shown in (a)

Regarding the magnetic properties of this material, these follow mostly from the magnetic Fe-atoms. According to [7], the magnetic moments of Fe-atoms in this ferromagnetic material are oriented along the c-axis. Moreover, the magnetic moment of the atoms at the $3g$-positions is significantly bigger than that of the $3f$-positions, with a reported 2.31 and 0.69 μ_B respectively [23]. The fact that two atoms of the same type carry such different magnetic moments in one material is referred to as mixed magnetism [24].

Liu et al. apply DFT-calculations to Fe_2P to gain information on the exchange interaction between the Fe-atoms at the different $3f$- and $3g$-positions [25]. From the exchange interaction graphs in figure 2, which plot the exchange interaction coefficients in Fe_2P against the distance between different atomic positions, some exchange interactions stand out. Firstly, the interactions between atoms at $3f$-positions are relatively weak. Secondly, the closest Fe-atoms within a $3g$-plane are strongly coupled by a positive coefficient. Between different $3g$-layers, however, there is very weak direct interaction. Thirdly, between neighboring $3f$- and $3g$-layers, there are several pairs with a positive exchange interaction, indicating that the magnetic moments in neighboring $3f$- and $3g$-layers tend to align parallel.

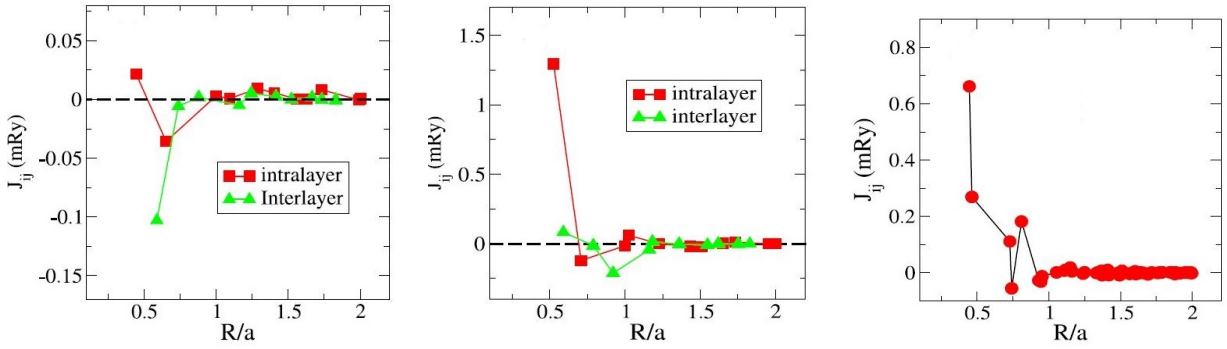

(a) (b) (c)

Figure 2: Distance dependence of the inter-site exchange interaction coefficients as computed in [25], normalized by the lattice constant $a = 5.81$ Å. (a) $3f$-$3f$ interactions (b) $3g$-$3g$ interactions (c) $3f$-$3g$ interactions.

The found values for the exchange interactions lead the authors to propose the following mechanism for the magnetic phase transition for Fe_2P. In the paramagnetic state, as Fe_2P approaches its T_C from above, the strong exchange interaction between the nearest neighbors within a $3g$-layer causes the magnetic moments of these atoms to be aligned. Due to this alignment, the positive interaction between $3f$- and $3g$-layers causes the former to become aligned with the latter. This coupling in its turn mediates the alignment of moments between different $3g$-layers, which would otherwise show little interaction. The result is a ferromagnetic state. This view on the interaction between magnetic moments of a mixed magnetic material such as Fe_2P around it T_C is proposed by Dung et al. as well [24]. In the DFT-calculations that are discussed in this thesis, it is thus of importance to see if we can get a hold of the exchange interaction coefficients during the lithiation of Fe_2P, as these terms are directly linked to the T_C of the material.

Part I

Modelling the lithiation of Fe_2P with DFT

3 Methodology

In the present section, the methodology of the first part of this thesis is presented. Firstly, the fundamental aspects of DFT and its implementation in the Vienna Ab Initio Simulation Package (VASP) are discussed. Thereafter, the approach to model the lithiation of Fe_2P and the magnetic phase transition of the resulting structure using VASP is discussed.

3.1 VASP

As has been stated, the first part of this thesis uses VASP software, an implementation of DFT, to perform energy-minimizing calculations on the crystal structure of lithiated Fe_2P. The details on DFT and VASP will not be discussed. However, some aspects that are essential for the interpretation of the results are discussed here.

Density Funtion Theory, a method of which VASP is an implementation, is applied to approximate the energy-minimizing configuration of the atoms in a lattice that solve the respective multi-body Schrödinger equation [26]. In DFT, the high-mass atoms in a material are fixed at a position and the degrees of freedom following from the movement of low-mass electrons reduced by dealing with an electronic density [27]. Discretization of this electronic density occurs by sampling the first Brillouin zone, the unit cell of k-space, the reciprocal of real space. Here, one selects a function-type, such as plane waves or Gaussian shapes [28].

The iterative procedure applied in VASP consists of a series of self-consistent steps. Within each self-consistent step, convergence of energy levels with respect to the electronic density at some fixed distribution of atomic positions is achieved [28]. Then, from round to round, the atomic positions are allowed to change as to achieve convergence of the final energies between rounds as well. One can choose to fix the lattice parameters or allow these to vary as well [28]. The result is an overview of the atomic positions and electronic density of the energy-minimizing structure at 0 K. Moreover, scalar magnetic moments can be presented for each atomic position.

From this very general description of the procedure, the most relevant parameters that enter into a VASP-calculation emerge. Namely, one enters a starting configuration of the atoms, as well as a starting magnetic moment at each position. Since the procedure of VASP, if it converges, converges to a *local* minimum, it is of utter importance that these initial guesses are somewhat close the global minimum. This can either be achieved by referring to experimental data on the respective crystal structure or by performing rough calculations over a wide range of lattice parameters and comparing the results.

Secondly, the user enters a set of sampling and convergence parameters [28]. Sampling parameters κ and σ indicate at which rate the electronic density is sampled, whereas the convergence limit indicates the maximum difference between the energies of two subsequent iterations below which VASP draws the conclusion that the calculations have converged.

3.2 Lithiation of Fe_2P

Through the use of VASP, the lithiation of Fe_2P has been modelled. In order to do so, a supercell of $2 \times 2 \times 2$ times the conventional unit cell as presented in figure 1 has been used. Using this supercell in stead of the conventional unit cell provides a higher number of possible locations that can be lithiated and accordingly allows for smaller steps in the lithiation process. However, the dimensions of the supercell are limited by the higher computational time required to perform calculations on bigger cells.

Departing from this structure, the preferred position of each next Li-atom in the supercell is established. The preferred position of a Li-atom is identified as the position of an Fe-atom

which, upon replacement, gives the lowest total energy for the supercell. Here, we exclude the possibility of a Li-atom substituting for a P-atom since experiments have found that lithium replaces Fe-atoms, and not P-atoms, in the structure of Fe_2P [9]. Moreover, the atomic radius of P-atoms is a lot smaller than the radius of Fe- and Li-atoms, leading us to expect the latter two types to be more likely to substitute for each other.

Since at each step in the lithiation process, there is a high number of possible positions for the next Li-atom, a sparse k-grid has been used. Moreover, the calculations for each structure were cut off after two self-consistent iterations. This approach is justified by the fact that, if one structure has a lower total energy upon convergence that another structure, the former generally has a lower energy than the latter after fewer iterations as well.

In the above procedure, at each step in the lithiation process the lattice parameters and atomic positions of the pure Fe_2P supercell have been used. Accordingly, it is assumed that the actual changes of the lattice parameters and relative positions of the atoms in the supercell do not dramatically influence the energies of the possible lithiated structures, such that conclusions with respect to the preferred position of each next Li-atom remain valid.

In order to draw conclusions as to whether a certain lithiated structure is viable in nature, the energy upon each step in the lithiation process is compared to the energy of the supercell with one Li-atom less. For the lithiation step to be physically admissible, the energy increase of the supercell must at least be lower than the energy difference between one Fe-atom and one Li-atom in their pure body centered cubic (bcc) state. This follows from the principle that the available atoms are arranged in such a way as to minimize the total energy.

3.3 Lithiated structure

As has been stated in chapter 2, experiments with lithiated Fe_2P have indicated that upon lithiation, the T_C of the material increases by 100-200 K [9]. Since lithium is a nonmagnetic material and iron is magnetic, this seems like a surprising results. Accordingly, it is of interest to see if ab-initio calculations on lithiated Fe_2P can be used to find an explanation for this behavior. Hence, the magnetic properties of the lithated structure will be studied and compared to the magnetic properties of pure Fe_2P.

Firstly, the development of the structural parameters throughout the process of lithiation is regarded. Since the magnitude of magnetic moments, as well as the magnetic exchange interactions between atoms of a kind are highly sensitive to the local environment of the respective atoms, as well as the distance between atoms, it is of importance to study the development of these factors upon lithiation. Moreover, a sensitivity of the T_C of hexagonal ferromagnets to the c/a-ratio is often reported (e.g. [29]). Accordingly, the development of the c/a-ratio is considered as well.

Secondly, the development of the magnetic moments at the $3f$- and $3g$- positions throughout the modelled lithiation is studied. Since the T_C of a ferromagnet is dependent on, among other factors, the magnetic moments of the atoms present in the respective material, it is relevant to see if the magnetic moments of the remaining Fe-atoms increase or decrease throughout the process of lithiation.

3.4 Magnetic transition

To model the magnetic transition of the lithiated structure, the energy corresponding to some artificial orderings of magnetic moments is calculated. In this approach, we stay within the constraints of VASP's settings of calculations with collinear magnetic moments. Here, VASP only returns the size and sign of magnetic moments, without specifying a direction. This is a

clear limitiation of the modelling technique that is used, since it limits the types of magnetic ordering that can be achieved. Moreover, since in general, VASP calculations converge towards formations corresponding to a local energy minimum, only a limited number of such artificial orderings of the magnetic moments can actually be achieved, namely those located near a local minimum. Adding to the fact that such orderings are very rough proxies of a paramagnetic state, VASP-calculations assume a temperature of 0 K, whereas the transition from a ferromagnetic to a paramagnetic state occurs at a finite temperature.

The primary condition on these orderings is that the sum of the magnetic moments over the supercell should approach zero, since we are looking to model a transition to a paramagnetic state. An approach is to model the paramagnetic state by an antiferromagnetic state, in which layers with alternating moments are placed along the direction of **c** [25] [30]. An alternative method is to cleverly group atoms in the plane spanned by **a** and **b** and the respective signs of their magnetic moments in order to achieve a net magnetic moment of zero.

By comparing the energy of such models for the paramagnetic state to the energy found for the structure with ferromagnetic ordering of magnetic moments, a proxy for the T_C of the lithiated structure is developed. Here, we can think of comparing the energy difference of the same ordering in the pure Fe_2P state and scaling this with the experimentally found T_C of pure Fe_2P to find an actual value for the T_C of its lithiated variant.

4 Results

In the following section, the results of the VASP-calculations that were performed to model the lithiation of Fe_2P are presented. General observations regarding the trends in these results are provided here, whereas a more in-depth discussion of the results is presented at the end of the chapter. The sampling and convergence parameters used for each of the calculations presented in this chapter can be found in table 12 in the Appendix.

4.1 Lithiation

The reader is reminded of the fact that a supercell of $2 \times 2 \times 2$ the conventional unit cell of Fe_2P is used in the following procedure. This implies that there are two $3f$-layers, containing 12 Fe-atoms each, and two $3g$-layers, containing 12 Fe-atoms each as well. Although the introduction of Li-atoms into this lattice breaks the symmetry of the supercell and references to $3f$- and $3g$-positions are factually no longer correct, these references are maintained for convenience.

Firstly, the energies of the supercell with one Li-atom at a $3g$-position, respectively a $3f$-position were calculated. The respective energies are -552.473 and -551.778 eV, indicating that the $3g$ position is preferred. This is in agreement with the experimental findings in [9].

Departing from a supercell with one Fe-atom at the $3g$-position replaced by a Li-atom, the energy of lithiation of each remaining Fe-position was approximated in accordance with the method presented in the previous chapter. In figure 3 on the following pages, the resulting energies of the supercell upon lithiation of the respective $3g$ positions are presented. It was found that the energy of the supercell upon introduction of a Li-atom at any of the $3f$-positions was always higher than the energies resulting from introduction of a Li-atom at any of the $3g$ position. The difference between the maximum energy of a structure with a Li-atom added to a $3g$-position and the minimum energy corresponding to a Li-atom added to a $3f$-position was always greater the 0.38 eV. Accordingly, the respective energies of lithiated $3f$-positions are not displayed.

In figures 3a to 3l on the following pages, we can identify a trend in the preferred position of the next Li-atom. Firstly, within the $3g$-layer in which lithiation has already occurred, the lowest energy is achieved by placing the next Li-atom near already lithiated positions. In the other $3g$-layer in the supercell, however, we observe the contrary trend. The positions directly above already lithiated positions give higher energies of the supercell than those positions that are not above the lithiated part of the other $3g$-layer. In general, minimal energy results from clustering the Li-atoms in one of the $3g$-layers. Eventually, all of the positions in one of the two $3g$-layers are filled with Li, whereas the other $3g$-layer, as well as the two $3f$-layers, contain no lithium.

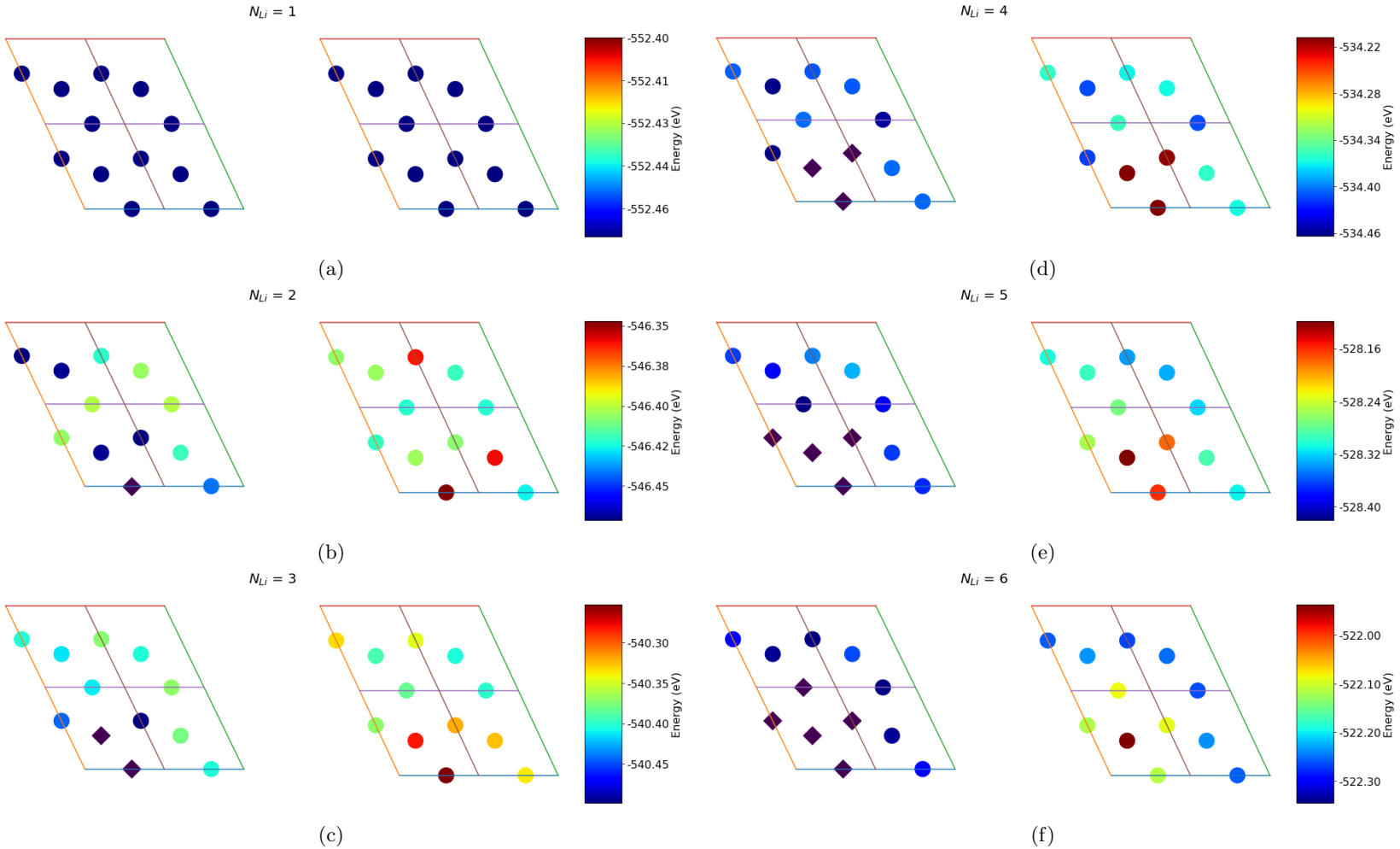

Figure 3: Unconverged energies of the supercell upon introduction of the next Li-atom at the positions marked by circles. Positions with a diamond have already been lithiated. In each spread, the left figure contains the $3g$-layer at $z = 0.25$, in which the first Li-atom was introduced. In the plots to the right, the $3g$-layer at $z = 0.75$ is displayed. Introduction of a Li-atom at $3f$-positions always led to total energies far above those presented here and are thus left out of this representation.

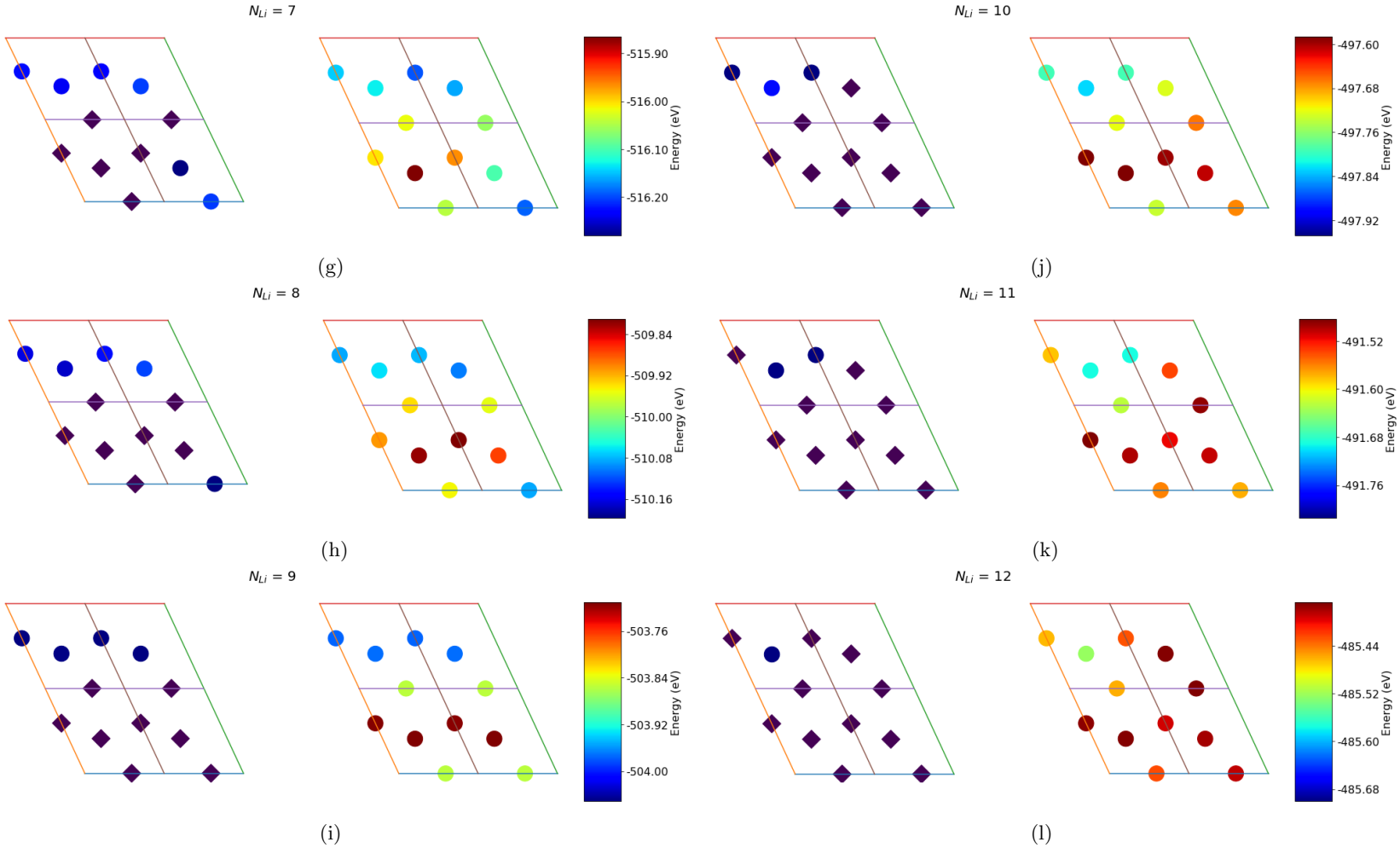

Figure 3: Continued, $N_{Li} = 7$ to $N_{Li} = 12$

The preference of lithium in occupying positions in a $3g$-layer over the $3f$-layers can be explained as follows. Firstly, Li has a bigger atomic radius than Fe, and far bigger than P, with calculated values of respectively 167, 156, and 98 pm [31]. Secondly, the distances of an Fe-atom at a $3f$-position to its nearest neighbors are considerably smaller than the respective distances for Fe-atoms at the $3g$-position. Fe-atoms at the $3f$-position have four neighboring P-atoms at a distance of 2.2-2.3 Å and two Fe-atoms in the same layer at a distance of 2.59 Å. Fe-atoms at the $3g$-position have five P-neighbors at 2.4-2.5 Å and four Fe-atoms in the same layer at 3.05 Å. Accordingly, assuming a position in the $3g$-layer provides a Li-atom with more space than occupation of a $3f$-position and thus results in a lower total energy. See table 3 in section 4.2 for the exact nearest neighbor-distances resulting from the computations.

4.2 Lithiated structure

All structures with the next Li-atom at the position found to be energetically favorable in the above calculations were relaxed, using the parameters that have been found to meet the convergence criteria in the case of the $2 \times 2 \times 2$ supercell of Fe_2P. The development of the total energy, lattice parameters and magnetic moments are now discussed.

Firstly, for further lithiation to be physically possible, the energy increase resulting from the replacement of an Fe-atom by a Li-atom in the supercell should at least be smaller than the difference in energy between an Fe-atom and a Li-atom in their pure bcc-forms, which is 6.33 eV. The change in energy of the supercell with respect to a supercell with one Li-atom less is displayed in figure 4. Here, it is clear the the energy increase of the supercell is far below 6.33 eV, making further lithiation physically viable at each lithiation step. This approach, however, does not take into consideration the possible formation of alternative materials, such as Fe_3P.

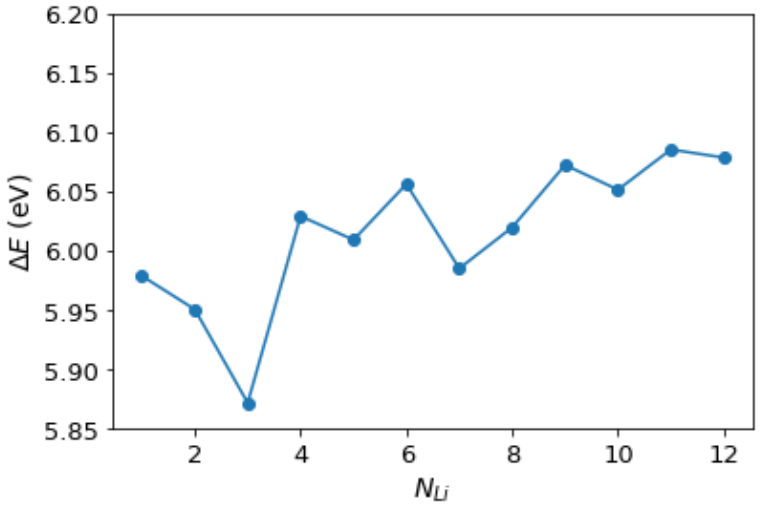

Figure 4: Energy difference at each step of the lithiation process with respect to a structure with one Li-atom less.

The non-monotonous trend in ΔE possibly follows from the fact that some of the intermediate structures are more symmetric than others, which could lead to a decrease in ΔE. A good example of such an occurrence is the structure with 3 Li-atoms (see figure 3d for the respective distribution), which regains a symmetry axis as compared to the structure with 2 Li-atoms.

For the pure Fe_2P structure, as well as the $Fe_{1.5}Li_{0.5}P$ structure, with one $3g$-layer lithiated, the energies over a selection of combinations of a and c were calculated. In figure 5, the respective results are presented. The equilibrium lattice parameters change significantly between the two structures. Whereas a increases upon lithiation, c decreases, leading to a shift of the c/a-ratio from 0.588 to 0.579. Referring to the reported sensitivity to the c/a-ratio of exchange interaction coefficients in general and T_C in specific, this shift in the c/a-ratio could possibly be associated with a change in T_C.

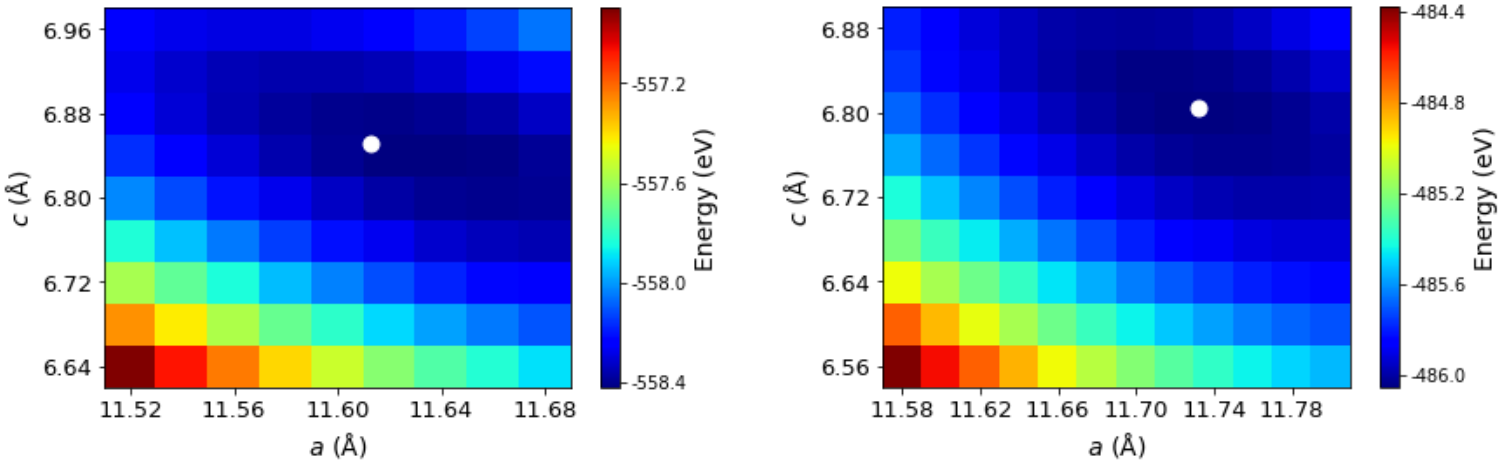

(a) (b)

Figure 5: Energies at combinations of a and c of (a) pure Fe_2P and (b) $Fe_{1.5}Li_{0.5}P$. Note that the values of a and c covered by the calculations are different for both structures. The parameter values for the structures after full convergence are indicated with a white dot. We observe an increase of a from 11.61 to 11.73 Å and a decrease of c from 6.849 to 6.807 Å due to the lithiation.

In figure 6, the development of the volume of the supercell and its c/a-ratio are displayed. It can be seen that the volume of the supercell increases monotonously upon the introduction of lithium, which is expected given the bigger atomic radius of Li over Fe [31]. On the other hand, the c/a-ratio decreases upon the introduction of Li, while this trend is not monotonous. This decreasing trend arguably follows from the fact that lithiation occurs in the a,b-plane, and a relative increase of a with respect to c is required to accomodate for this addition of atoms with a bigger radius.

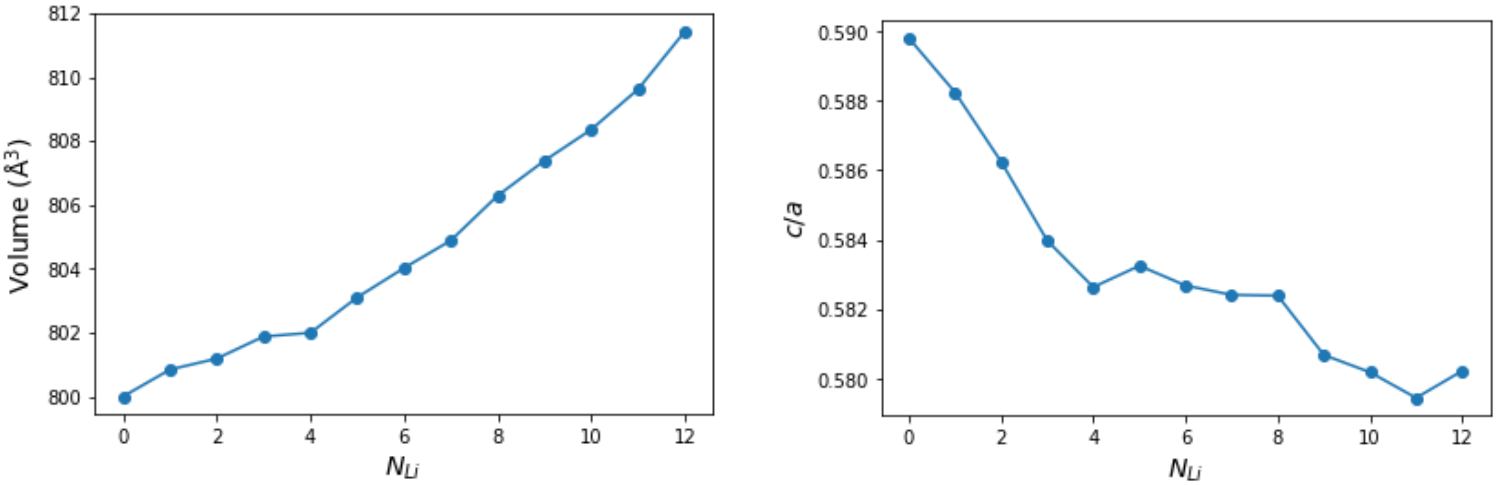

(a) (b)

Figure 6: The development of (a) the supercell's volume and (b) the supercell's c/a-ratio as a function of the number of Li-atoms in the supercell.

Given the symmetry of the supercell of $Fe_{1.5}Li_{0.5}P$ in the a, b-plane, we can identify a unit cell smaller than the respective supercell that was used to model the process of lithiation. Here, compared to the conventional unit cell of pure Fe_2P, we still have a doubling along **c**, since now the $3g$-layers along this direction are alternatingly occupied by Li- and Fe-atoms. In the supercell, in the plane spanned by **a** and **b**, we identify 2x2 times the repeated cell as presented in figure 7

As has been stated above, the introduction of Li-atoms into the structure of Fe_2P breaks the symmetry of the supercell, rendering the references to the Wyckoff positions $3f$ and $3g$ for Fe and $1b$ and $2c$ for P in space group 189 incorrect. We now continue to consider the symmetry of the newly conceived structure, $Fe_{1.5}Li_{0.5}P$.

The new unit cell shows great resemblance to the unit cell of Fe_2P. Obviously, **c** of this new unit cell is roughly two times as long as in the unit cell of Fe_2P. At first sight, one might think that the alternating layers of Li and Fe in the former $3g$-layers reduces the number of symmetry transformations allowed on this structure. However, if we consider the atomic positions with respect to the plane $z = 0.25$ (in stead of $z = 0$), we see that actually the exact same set of transformations towards which our $Fe_{1.5}Li_{0.5}P$ structure is symmetric is allowed as on Fe_2P. The Wyckoff positions of the respective atoms are, however, different [21]. These positions are presented in table 2.

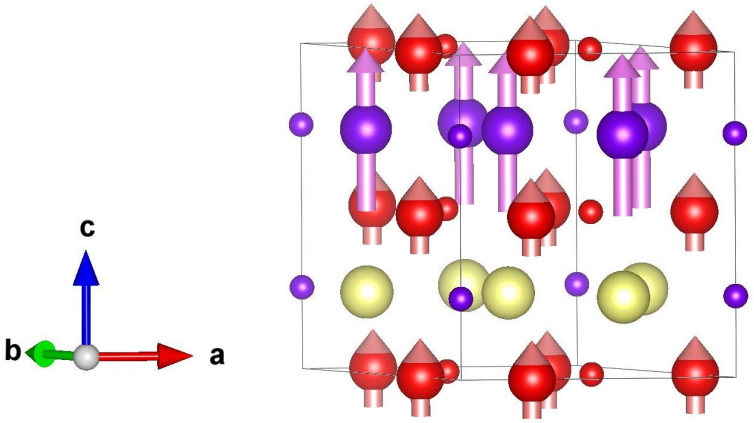

Figure 7: Unit cell of $Fe_{1.5}Li_{0.5}P$. The big red and purple spheres represent Fe-atoms at the $3f$- and $3g$- positions, respectively. Small red and purple spheres represent P-atoms at the $2c$- and $1b$-positions, respectively, and the yellow spheres are Li. The magnetic moments of Fe at $3f$ and $3g$ are respectively 0.65 and 1.99 μ_B. The small induced moments on the remaining atoms are not shown.

Table 2: Wyckoff positions of the atoms in $Fe_{1.5}Li_{0.5}P$, which is part of space group 189 [21]. Here, the plane containing Li-atoms is taken as $z = 0$. Positions with a degree of freedom in the value of x or z are denoted with the respective value as found through the computations in VASP. Moreover, $a = 5.866$Å and $c = 6.807$Å.

Atom	Wyckoff Position	Coordinates	x	z
Fe	$6i$	(x,0,±z), (0,x,±z), (-x,-x,±z)	0.257	-
P	$4h$	($\frac{1}{3}$, $\frac{2}{3}$, ±z), ($\frac{2}{3}$, $\frac{1}{3}$, ±z)	-	0.263
Li	$3f$	(x,0,0), (0,x,0), (-x,-x,0)	0.591	-
Fe	$3g$	(x,0,$\frac{1}{2}$), (0,x,$\frac{1}{2}$), (-x,-x,$\frac{1}{2}$)	0.595	-
P	$1a$	(0,0,0)	-	-
P	$1b$	(0,0,$\frac{1}{2}$)	-	-

In table 3, the distances between the Fe-atoms in the $3f$- and $3g$-layers and their nearest neighbors in Fe_2P and $Fe_{1.5}Li_{0.5}P$ are presented. Since both the magnetic moments of the atoms in a material and the exchange interactions between the respective atoms are highly sensitive to the local environment of the atoms, it is relevant to consider the change in the local environment of the magnetic Fe-atoms. It appears that in most of the cases, interatomic distances increase, which is not unexpected since the volume of our unit cell increases upon lithiation. Decreases in interatomic distances occur between Fe-atoms in the $3g$-layers and P-atoms in the neighboring $3f$-layers, from 2.454 to 2.403 Å, and between Fe-atoms at the $3f$- and $3g$-positions, going from 2.693 to 2.687 Å. Referring to the finding in [25] that the interaction between the $3f$- and $3g$-positions is decisive for the magnetic behaviour of Fe_2P, the decrease of the distance between these positions could have implications towards the magnetic behaviour of $Fe_{1.5}Li_{0.5}P$.

Table 3: Interatomic distances d for the Fe-atoms at the $3f$- and $3g$-positions in Fe_2P and $Fe_{1.5}Li_{0.5}P$. The subscripts 1, 2, and 3 represent, respectively, whether a neighbor is located in a $3f$-layer, a $3g$-layer containing Fe-atoms, or a $3g$-layer containing Li-atoms. The multiplicity of each neighbor is indicated by the integer preceding the atomic type.

$3f$				$3g$			
Fe_2P		$Fe_{1.5}Li_{0.5}P$		Fe_2P		$Fe_{1.5}Li_{0.5}P$	
Neighbor	d (Å)	Neighbor	d (Å)	Neighbor	d (Å)	Neighbor	d (Å)
2 P_1	2.190	2 P_1	2.217	1 P_2	2.373	1 P_2	2.375
2 P_2	2.272	1 P_2	2.270	4 P_1	2.454	4 P_1	2.403
		1 P_3	2.274	2 Fe_1	2.587	2 Fe_1	2.614
2 Fe_2	2.587	1 Li	2.600	4 Fe_1	2.693	4 Fe_1	2.686
		1 Fe_2	2.614	4 Fe_2	3.045	4 Fe_2	3.089
2 Fe_1	2.587	2 Fe_1	2.608				
4 Fe_2	2.693	2 Fe_2	2.687				
		2 Li	2.703				

The approach to model the lithiation for Fe_2P has, until now, always considered the next preferred position for an additional Li-atom, and compared the marginal energy increase of the supercell to the energy difference between Fe and Li in their respective pure bcc states. The observed trend was that the Li-atoms tend to group together in a $3g$-layer. It could well be, however, that due to different mixing entropies, a supercell with a fully lithiated $3f$-layer has a lower energy than our lithiated structure with one $3g$-layer filled with Li. Moreover, it can be informative to perform some boundary checks on the energies of a structure with two lithiated $3g$-layers, and a structure with both a $3f$- and $3g$-layer lithiated. The respective energies are presented in table 4.

Table 4: Energies of structures with the indicated percentages and planes of lithiation. A 50% filling rate of $3f$ or $3g$ implies that one out of the two layers of the respective kind is lithiated.

Structure	Pure	50% $3g$	50% $3f$	100% $3g$	50% $3g$, 50% $3f$
Energy (eV)	-558.45	-486.26	-478.40	-409.02	-409.51 height

The calculated energies confirm that also in the case of fully lithiated layers, the $3g$-layer is energetically preferable. Moreover, proceeding the lithiation from our structure with one $3g$-layer filled, we see that lithiation is no longer energetically favorable. Each added Li-atom leads to an energy increase of the supercell of on average 6.44 eV and 6.40 eV in the cases of respectively lithiation of another $3g$-layer, or one of the two empty $3f$-layers. Both these average energy differences are higher than the energy decrease due to the difference in pure state energies of Fe and Li, being 6.33 eV.

As has been stated, the above calculations serve merely as boundary checks. Actually, the further we proceed the process of lithiation, the less likely it becomes that our assumption of the supercell retaining its hexagonal shape holds. In fact, first-principle calculations of FeLiP indicate that this structure is no longer of the hexagonal space group, but in the tetragonal $p4/nmm$ space group [32] [33]. Such changes in the space group are difficult to account for in the absence of experimental data on a certain structure, other than heuristic trial-and-error methods. It cannot be excluded that a change in space group occurs already at an earlier stage of the modelled lithiation process.

Taking into account this remark, we conclude the following findings with respect to the

structural development of the supercell upon lithiation. Firstly, the preferred occupation follows a pattern in which clustering of Li-atoms occurs in the a, b-plane. Secondly, as a result of this lithiation, we observe a decrease of the c/a-ratio. Lastly, a reorientation of the atoms in the unit cell leads to an increase of most of the interatomic distances, since the supercell volume increases, while the distance between Fe-atoms at the $3f$- and $3g$-positions forms a noteworthy exception. The following section turns to discuss the development of the magnetic moments of the Fe-atoms throughout the process of lithiation.

4.3 Magnetic moment development

In figure 8, the development of the magnetic moments at the $3g$ and $3f$-positions is presented. At both positions, we observe a decrease in the magnetic moment. From Fe_2P to $Fe_{1.5}Li_{0.5}P$, the moment at the $3g$-position goes from 2.23 to 1.99 μ_B, a 10.8% decrease, whereas the moment at the $3f$-position goes from 0.83 to 0.65 μ_B, a 21.6% decrease. However, due to the asymmetry introduced in the supercell in all but the pure and fully lithiated case, we also see that at some positions the magnetic moment is actually higher than the starting moment.

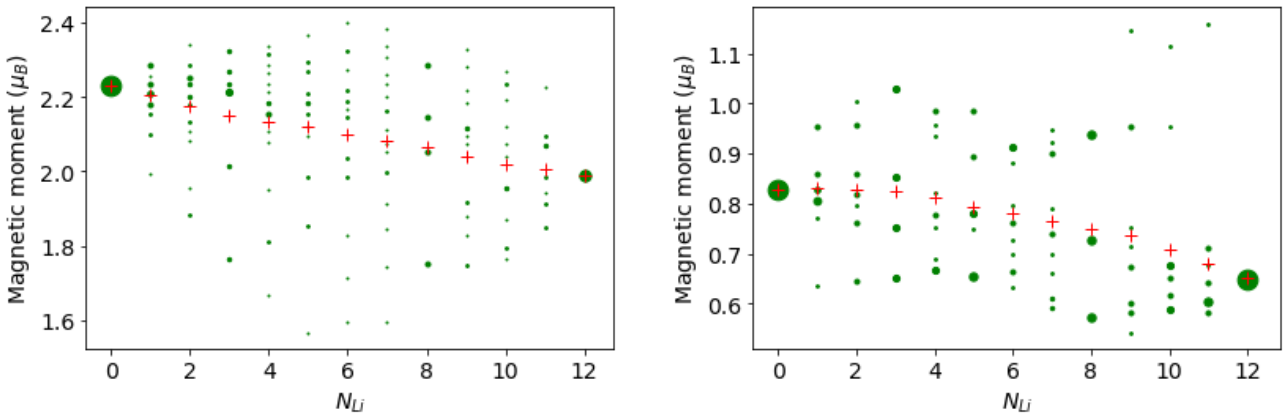

(a) (b)

Figure 8: The development of the spread of magnetic moments at the (a) $3g$-positions and (b) the $3f$-positions (circles), as well as the average over the respective positions (pluses) . Here, the area of a circle scales with the number of positions in the supercell sharing the respective moment. It should be noted that, since the total number of $3g$-positions decreases upon lithiation, the total area in (a) decreases upon lithiation. For both the $3g$- and $3f$-positions, the magnetic moments show a decreasing trend.

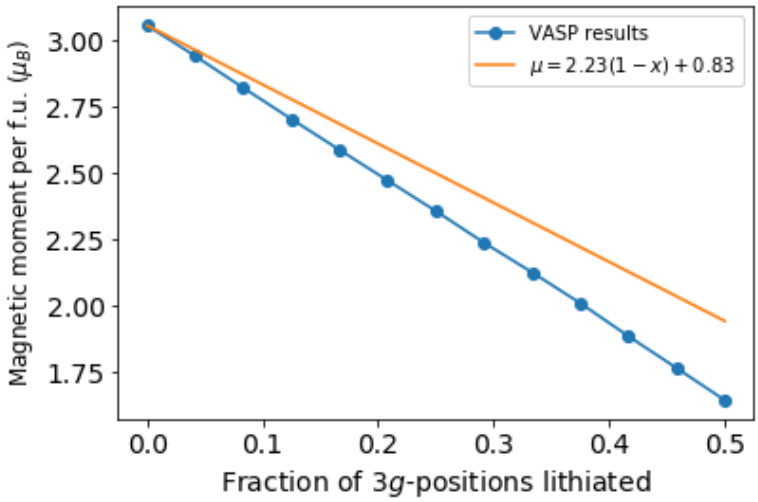

Figure 9: The total magnetic moment averaged per formula unit of $(\mathrm{Fe}, \mathrm{Li})_2\mathrm{P}$. The upper line indicates the development of the magnetic moment due to the mere reduction of magnetic Fe-positions in the $3g$-layer, under the conservation of the initial moments of 2.23 and 0.83 μ_B for the remaining Fe-atoms at $3f$- and $3g$-positions, respectively.

For both positions, we thus observe that the magnetic moments of the remaining Fe-atoms tend to decrease due to the reduction of the number of magnetic Fe-atoms at the $3g$-positions. The fact that the relative decrease in the magnetic moment of Fe at the $3f$-positions is greater than at the $3g$-positions corresponds with the findings in [25] that the moments at the former positions result from strong interaction with the moments at the $3g$-positions. The reduction of the number of the latter positions thus logically leads to a reduction of the moments of Fe at the $3f$-positions. On the other hand, Fe at $3g$-positions carry a moment that pertains, although sensitive to interlayer interaction with the $3f$-positions, more independently, due to strong intralayer interaction with other $3g$-positions.

The magnitude of the magnetic moments in a structure contribute to the T_C of the respective material. However, other factors, most notably the strength of the exchange interactions between the magnetic atoms, influence this transition temperature as well (see section 2.2). Thus, the monotonous decrease in magnetic moments of Fe-atoms at the $3f$- and $3g$-positions do not necessarily imply a decrease in the T_C of the supercell. In the following section, the present work turns to proxy this transition temperature by modelling a paramagnetic state for the newly conceived structure $\mathrm{Fe}_{1.5}\mathrm{Li}_{0.5}\mathrm{P}$.

4.4 Magnetic phase transition

4.4.1 Antiferromagnetic ordering along c-axis

To model the magnetic phase transition of $Fe_{1.5}Li_{0.5}P$, firstly an antiferromagnetic ordering along the c-axis has been constructed by stacking two unit cells along this axis. Here, we can see that the two segments consisting of a $3f$-,$3g$-, and $3f$-layer are seperated by the lithiated $3g$-layers. The two segments were given opposite directions of magnetic moments. The energy of this structure is -243.20 eV, which is actually lower that the energy of -243.12 eV of the corresponding structure with a ferromagnetic ordering. This suggests that for our lithiated structure, the respective antiferromagnetic ordering is energetically favorable and is the actual ground state.

To test whether this conclusion is likely to hold for temperatures above 0 K, a thermal expansion was simulated by calculating the energy for both orderings at an increasing volume of the unit cell. In figure 10 energies of both structures are plotted against the length of the a-axis, with the c/a-ratio fixed at the value of the corresponding converged structures. For pure Fe_2P, the difference between the volume at 0 K found through VASP and the volume at room temperature found experimentally in [9], is about 1%. For $Fe_{1.5}Li_{0.5}P$, this corresponds to an increase of a to around 5.91 Å. Here, the energy of the antiferromagnetic ordering of our lithiated structure is still lower than the energy of the ferromagnetic ordering, suggesting that also at nonzero temperatures, for example room temperature, the former would be preferred. See figure 10 for the respective results.

The size of the magnetic moments of Fe-atoms at the $3f$-positions is 0.66 and 0.74 μ_B for the FM- and AFM-ordering, respectively. At the $3g$-positions, the relative difference is smaller, with moments of 2.00 and 2.02 μ_B, respectively. This suggests that the net interaction between the $3g$-layer and $3f$-layers from the two different sections is negative, such that the moments at $3f$-positions have a bigger size if the moment of the $3g$-layer in the other segment is of opposite sign. This also explains for the lower energy of the AFM-structure.

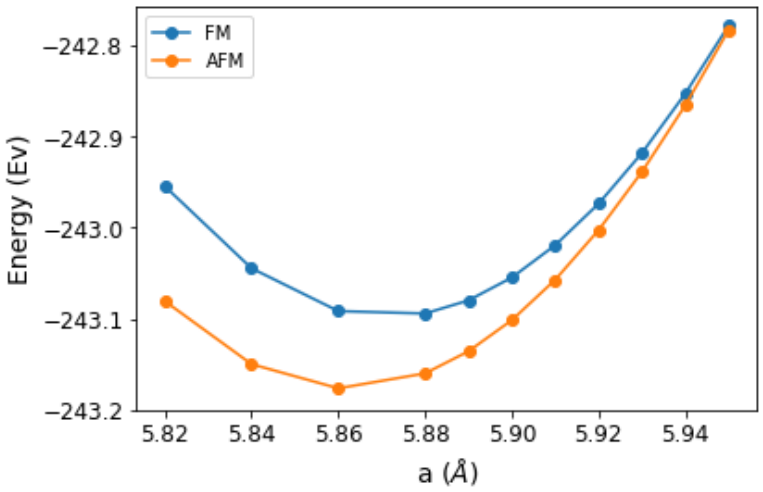

Figure 10: Energies for the ferromagnetic and antiferromagnetic orderings of $Fe_{1.5}Li_{0.5}P$ along the c-axis, as discussed in the text, with increasing volume and c/a fixed at the value corresponding to the energy-minimizing structure.

4.4.2 Antiferromagnetic order in a,b-plane

The above results do not provide us with any measure for the T_C of the lithiated material. The results actually indicate that, for this highly artificial structure with perfectly alternating $3g$-layers filled with Li- and Fe-atoms, respectively, the ferromagnetic state is not the energy-minimizing ordering of magnetic moments.This is the result of the fact that, by substituting one $3g$-layer of Li-atoms for Fe-atoms, we effectively isolate the segments as identified above. The interaction between these segments is apparently weakly negative.

It is more interesting to look at structures with alternating moments within these same segments. To do this, we return to the supercell with $2 \times 2 \times 2$ the dimensions of the unit cell of Fe_2P we worked with before. Several types of order of the magnetic moments in this structure were tested, but it appeared calculations only converged fully when orderings were imposed that followed the triangular groups of $3g$-positions as indicated in figure 11.

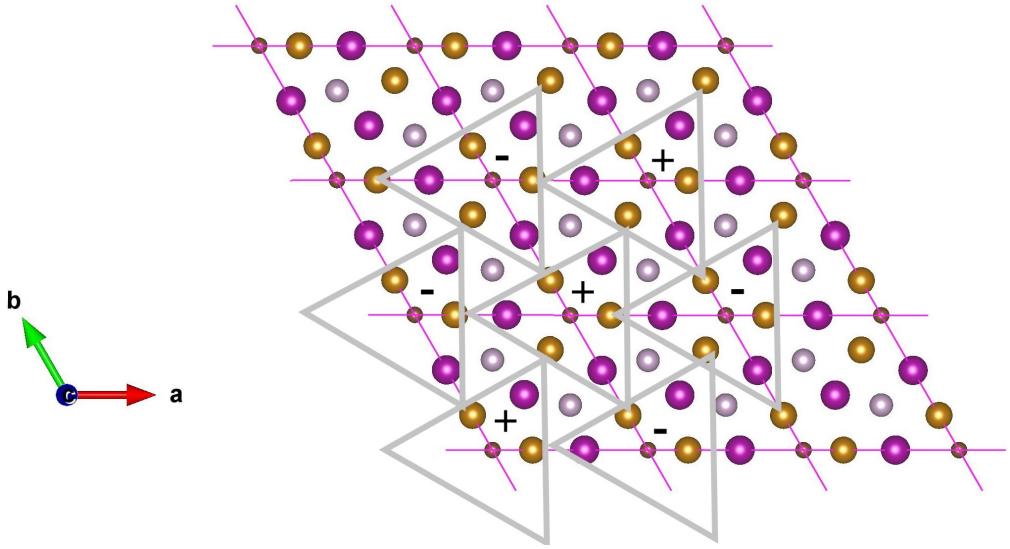

Figure 11: The ordering of $3g$-moments as discussed in the text. All atomic positions in the supercell along the c-axis have been collapsed into one plane. Purple spheres indicate $3g$-positions, gold the $3f$-positions and the remaining spheres indicate positions of P in the two different layers.

From this ordering of moments of Fe-atoms at the $3g$-position, we still have two options to set the moments at the $3f$-positions. These moments can be set to couple to the two $3g$-positions that neighbor the $3f$-position within the indicated triangles, as indicated in figure 12a. A second option is to give the $3f$-positions the same sign as the $3g$-position that actually has the shortest distance to this $3f$-position, its nearest neighbor, as presented in 12b.

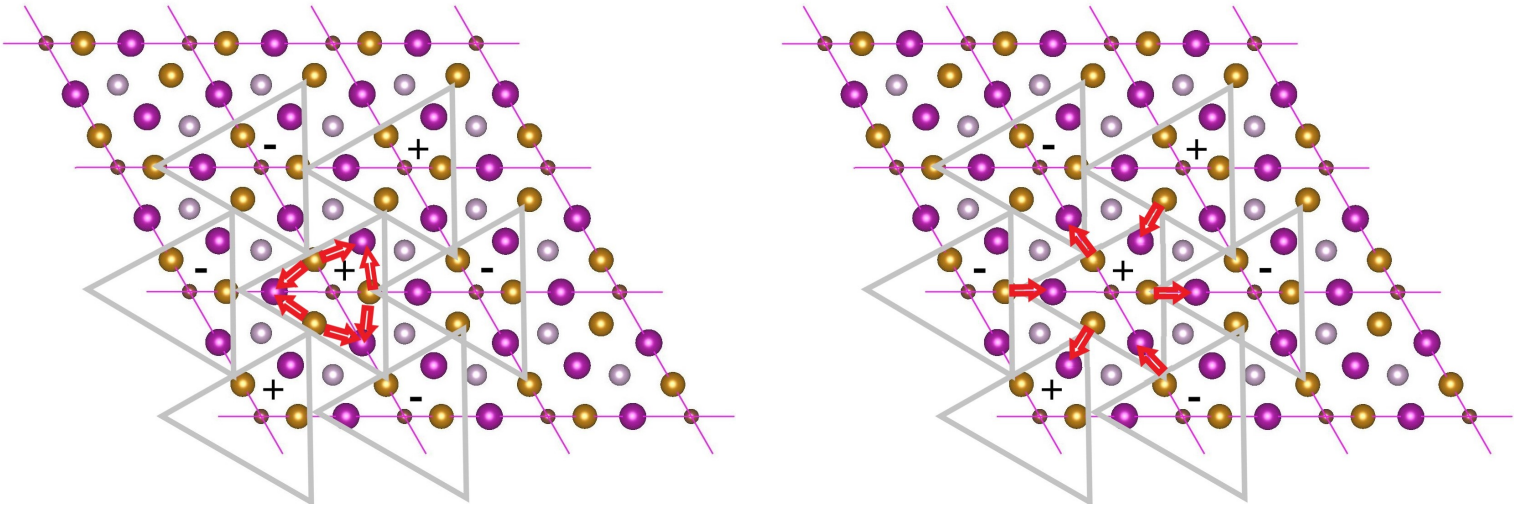

(a) (b)

Figure 12: The two orderings of the magnetic moments at the $3f$-positions. In (a) moments couple to the moments of the two neighboring $3g$-positions within the triangles, which are actually the next nearest $3g$-neighbors of the $3f$-positions. In (b), the moments at the $3f$ position are coupled to the moment of their nearest $3g$-neighbor. The arrows indicate to which $3g$-positions the $3f$-positions are coupled in terms of the alignent of their magnetic moment.

For $Fe_{1.5}Li_{0.5}P$ both these structures converged. The energy of the structure in figure 12a, using the lattice parameters of the structure in ferromagnetic ordering,is -484.80 eV. For the structure in figure 12b, the energy was -484.54 eV. The energy under ferromagnetic ordering is -486.26 eV.

The energy differences are an order of magnitude bigger than the energy difference between the FM- and AFM-ordering in section 4.4.1. This indicates that the magnetic exchange interactions that these triangle orderings are directed against are significantly stronger than the exchange interactions between the segments in the stacked unit cell of section 4.4.1.

To get a reference point for these energy differences and their possible translation into a T_C for the lithiated material, the same triangle-orderings were imposed on the supercell of pure Fe_2P. It was found that the next-nearest-neighbor-ordering from figure 12a could not be converged. Or rather, moments would always flip to the nearest-neighbor-ordering from figure 12b. The energy of this structure is -555.34 eV, compared to an energy under ferromagnetic ordering of -558.45 eV.

The energies corresponding to this triangle-grouping of moments were also computed for structures with $\frac{1}{3}$ and $\frac{2}{3}$ of one of the $3g$-planes lithiated. Fotunately the corresponding structures, when subjected to a triangle-grouping of the moments of the remaining Fe-atoms at the $3g$-positions, both contained equal numbers of these Fe-atoms with a positive and a negative magnetic moment. Accordingly, the net magnetic moment of both structures was approximately zero under the paramagnetic ordering. A small deviation from zero was observed as a result of the high level of asymmetry in the respective supercells. The resulting energies are presented in table 5.

Table 5: Energies at different lithiation-levels in the proxies of the paramagnetic state, the orderings corresponding to 12b (E_{nn}) and in 12a (E_{nnn}).

	$Fe_{1.5}Li_{0.5}P$	Fe_2P	$Fe_{1.83}Li_{0.17}P$	$Fe_{1.67}Li_{0.33}P$
E_{FM}(eV)	-486.26	-558.45	-534.62	-510.55
E_{nn}(eV)	-484.54	-555.34	-531.86	-508.47
E_{nnn}(eV)	-484.80	-	-	-
ΔE(eV)	1.72	3.11	2.76	2.08

Comparing $Fe_{1.5}Li_{0.5}P$ with pure Fe_2P, two things draw the attention. Firstly, the fact that for Fe_2P, the ordering from figure 12a cannot be imposed, whereas for $Fe_{1.5}Li_{0.5}P$ it actually has a lower energy than the other ordering, indicates a shift in the magnetic exchange interactions. We will come back to this later. Secondly, the energy difference of the nearest-neighbor-structure with respect to the ferromagnetic state is 1.76 eV for $Fe_{1.5}Li_{0.5}P$, significantly smaller than the 3.11 eV for Fe_2P.

The energy differences between the ferromagnetic state and the model of the paramagnetic state, which serve as a proxy for the T_C of the corresponding structures, are presented in figure 13. The development shows a remarkable resemblance to a hypothetical development of ΔE, were this a linear function that is equal to the measure ΔE at a lithiation fraction of 0, going to a ΔE of 0 if all $3g$-positions are lithiated. This suggests that the T_C, within our modelling approach, is a linear function of the number of $3g$-positions containing Fe. This is corroborated by the fact that FeLiP, a structure with all $3g$-positions lithiated, is nonmagnetic in VASP and would thus have an associated ΔE of 0.

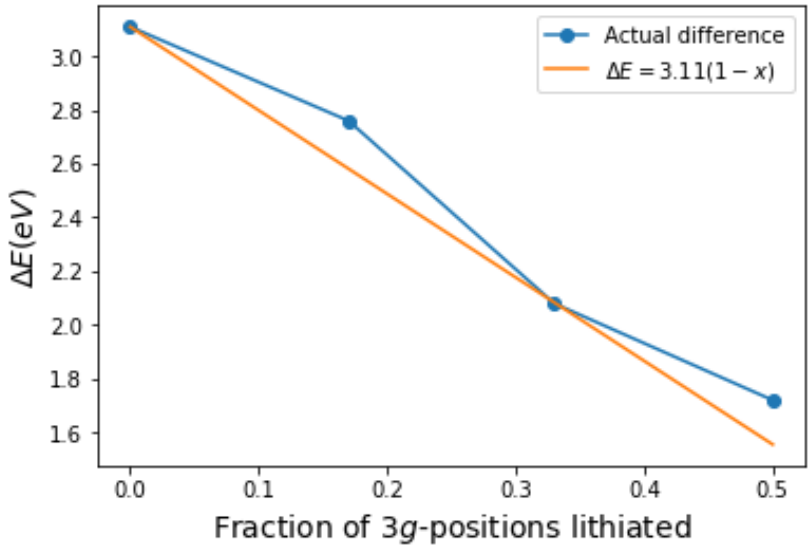

Figure 13: Proxy of T_C plotted against the fraction of lithiated $3g$-positions. The straight line represents the development of ΔE if this were a linear function in the lithiation fraction.

4.5 Discussion

The objective of this part of the present report has been twofold. Firstly, the structural development of a Fe_2P-supercell upon the replacement of Fe-atoms by Li-atoms was modelled, as well as the development of the magnetic moment in the respective structures. Secondly, it was the objective to derive a proxy for the T_C at different steps in this lithiation process. Here, the energy of a supercell with a ferromagnetic ordering of magnetic moments was compared to that of the same structure with an antiferromagnetic order of the moments in the plane spanned by **a** and **b**.

Regarding the pattern observed in the lithation of the supercell, we can make some remarks as to the validity of this procedure. Firstly, the selection of the size of the supercell is limited by the increase of computational time corresponding to a bigger cell. The bigger the supercell, the better the simulation can be expected to correspond to reality. Secondly, throughout the process of selecting the preferred position of a next Li-atom, the lattice parameters corresponding to the unit cell of pure Fe_2P were used. However, we have also observed that lithiation significantly influences the lattice parameters and relative atomic positions. Accordingly, it is possible that the found preferred positions actually lead to higher energies than alternative structures if we would let all structures relax fully. Again, here the procedure is limited by the increase in computational time that this would entail.

Lastly, the modelled lithiation as compared to the process of lithiation as it occurs in nature is highly artificial. The periodicity of the lithiation, for example, does not correspond to the fact that in nature, the effect of introduction of a foreign element is a lot more local. Accordingly, the filling up of alternating layers in the a,b- plane with lithium is something unlikely to happen in reality. Here, we would expect clusters of Li-atoms to occupy parts of $3g$-layers. Moreover, the presence of a cluster of Li-atoms at a significantly big distance in the lattice should not have too big an influence on the probability that certain $3g$-positions will be lithiated.

Let us now consider the method used to proxy T_C for the pure and lithiated structures. Although this method has given us a suggested development of the T_C, it is a rather brute-force method. More delicate, advanced methods seek to derive T_C through the exchange interaction coefficients between the atoms in a material of interest. Knowing these coefficients, in combination with the size of the magnetic moments at different (symmetrically) unique positions in a material, one can derive a value for T_C. The derivation of this approach is nicely formulated in [14].

Although a more advanced methodology is generally used to calculate the exchange interaction coefficients through ab-initio calculations, attempts have been made in the present research to approximate these coefficients for our lithiated structure. These attempts served to calculate the energies of $n + 1$ orderings of magnetic moments. In doing so, a linear system of equations could in principle be established, in which the exchange interaction coefficients are the unknowns.

Based on the fact that in pure Fe_2P, there are 11 'strong' interaction terms [25], 4 of which are not relevant to our $Fe_{1.5}Li_{0.5}P$ because of the lithiation of one full $3g$-layer, one could hope that calculating $11 - 4 + 1 = 8$ different structures would suffice to approximate the strongest exchange interactions. However, notwithstanding an extensive effort in which many combinations of magnetic moment directions with a total sum of zero were tried, only the triangular orderings resulted in a nicely converged structure, owing to the coincidence of the structural symmetry and the symmetry of the magnetic moment orderings in these cases. Accordingly, the tried method did not result in any useful approximations of the exchange interaction coefficients.

The experimental result from [9], suggesting that the T_C of Fe_2P increases upon lithiation, has not come forward in the calculations presented in this report. The experimental result is rather counter-intuitive, as one would not necessarily expect the replacement of magnetic Fe-

atoms at the $3g$-site by non-magnetic Li-atoms to lead to an increase of the T_C. However, this could still be the effect as structural parameters are affected, the local environment of the respective magnetic positions change, possibly leading to stronger magnetic exchange interaction between the remaining Fe-atoms. Again, this is not something that results from the performed calculations. This divergence from the experimental findings could for example be the result of the fact that the lithiation fraction of our final structure of 25% is higher than what was achieved in [9]. Although an as prepared lithiation percentage of 25% is noted in [9], it is quite likely that the actual fraction of lithium included into the structure was a lot lower. Accordingly, the present focus on $Fe_{1.5}Li_{0.5}P$ might have been far from the experimental reality. Moreover, for lower lihiation fractions, it might well be that other proxies for a paramagnetic states converge and serve as a better proxy for the respective state.

The calculations of the two possible orderings of magnetic moments as presented in 12a and 12b, in which the moments of the Fe-atoms at the $3f$-positions coupled to the nearest or the next nearest Fe-neighbor in the $3g$-layer, do suggest us with a possible change in the relative strengths of the respective exchange interactions. In pure Fe_2P, it was not possible to couple the moment of $3f$-positions to their respective next nearest $3g$-neighbors, rather than to their nearest neighbor. In $Fe_{1.5}Li_{0.5}P$, this is possible and actually gives a lower energy than the coupling to the nearest $3g$-neighbors. This suggests that as a consequence of the lithiation, the exchange interaction between $3f$-positions and their next nearest $3g$-neighbors increases relatively to the interaction with the nearest $3g$-neighbor. More advanced methods could be addressed to get values for these exchange interaction coefficients.

Part II
Modelling structural phase transitions with FEM

5 Model development

The Finite Element Method (FEM) is a numerical method often applied to spatial problems in which the domain does not posses a convenient geometry, or when discretization of the respective domain is desired to be non-uniform over the domain [34]. The principle of this method rests in subdividing a problem into elements, finite subdomains, on which the solution to a problem, often a partial differential equation or a minimization problem, is approximated. In the following subsections, some general concepts regarding the FEM are introduced. For a more extensive treatment of these concepts the reader is referred to [34] and [35]. Hereafter, the respective concepts are applied to a minimization problem that is developed to model the magnetostructural phase transition of a 2D material.

5.1 From minimization problem to linear algebra

Given is a problem of the general form of equation 8, defined on some domain Ω. Here, u is an unknown function on Ω, returning f when subjected to the linear operator L, and u is subject to a specified set of boundary conditions on $\partial\Omega$.

$$L(u) = f \tag{8}$$

If u satisfies equation 8, then for any $v(\mathbf{x})$,

$$\int_\Omega L(u)v(\mathbf{x})d\mathbf{x} = \int_\Omega f(\mathbf{x})v(\mathbf{x}))d\mathbf{x} \tag{9}$$

Accordingly, if not readily present in the form of a minimization problem, we urge to transform a problem of the form in equation 8 into the general form of a minimization problem by minimizing the difference between the two integrals in equation 9. Here $\sum$ denotes the set of admissible functions in this minimization problem.

$$\min_{u\in\sum} J(u) = \int_\Omega F(u)d\mathbf{x} \tag{10}$$

Let us now approximate u by considering subset subset $\sum_h$ of $\sum$, formed by the linear combinations of a finite set of basis functions, which can be selected based on the geometry and form of the respective problem, as presented in equation 11 [35]. We let the basis functions $\phi_i(\mathbf{x})$ satisfy the homogeneous type of the boundary conditions of the original problem.

$$u^n(\mathbf{x}) = \sum_{j=1}^{n} a_j\phi_j(\mathbf{x}) \tag{11}$$

Now, we look for a linear combination of basis function minimizing the error term according to equation 12. Evidently, we select $u(\mathbf{x})$ in the place of $v(\mathbf{x})$.

$$\min_{u\in\sum_h} J(u) = \int_\Omega (L(u)u(\mathbf{x}) - f(\mathbf{x})u(\mathbf{x}))d\mathbf{x} \tag{12}$$

Now, given a minimization problem of the form in equation 12 and a set of basis functions subject to appropriate boundary conditions, we look for a linear combination of these basis functions of the form in 11 which minimizes the defining integral. Thus, the first derivative with respect to each coefficient a_i must equal zero.

$$\frac{\partial}{\partial a_i}\int_\Omega F(u^n(\mathbf{x}))d\boldsymbol{x} \tag{13}$$

Here, upon selection of proper basis functions, which should be orthogonal and equal to zero in most parts of the domain, we can derive a problem of the form in equation 14. Due to the fact that the basis functions are equal to zero in most elements, and accordingly orthogonal to most other basis functions, the so-called stiffness matrix $\mathbf{S}$ will generally be sparse. $\mathbf{f}$ processes the forcing terms and $\mathbf{a}$ contains the coefficients we wish to solve for to approximate the solution to the problem at hand. For a non-singular, thus invertible matrix S, we can consequently find a solution to the approximation problem.

$$\mathbf{Sa} = \mathbf{f} \tag{14}$$

5.2 Stress and strain, potential energy

In general, a function $u(\boldsymbol{x})$ subject to the FEM can define any quantity that is a function of the spacial coordinate $\boldsymbol{x}$. Accordingly, the FEM is abundantly applied to the heat equation, the Navier-Stokes equations for fluid flow and other problems, often with domains making the application of other techniques, such as the Finite Difference Method less appropriate for application [34].

We turn, however, to the category of continuum mechanics, in which the equations for stress and strain govern the form assumed by a solid [34][36]. The key objective here is to process the influence of the discontinuous change of equilibrium dimensions of subdomains, or *grains*, in a 2D solid body as a result of a magnetostructural phase transition.

Let us consider a 2D body and its displacement field $\mathbf{u}(x,y) = \begin{Bmatrix} \mathrm{u(x,y)} \\ \mathrm{v(x,y)} \end{Bmatrix}$. Given such a displacement field, an infinitesimal part of the body with the initial location (x,y) has a position given by equation 15.

$$(x', y') = (x + u(x,y), y + v(x,y)) \tag{15}$$

Now, one can imagine that, is one to move a body in its entirety by some u_0, this does not influence the body as it would correspond to a mere change of the point of reference. However, when the dislocation is not constant throughout a body, this causes nonzero derivatives of the displacement, which are accounted for by the strain tensor[35][36]. The relation between strain and the dislocation vector of a body is accounted for by a differential operator, according to equation 16. As has been stated, we limit our consideration to the 2D case of plane strain for now.

$$\boldsymbol{\varepsilon} = \begin{Bmatrix} \varepsilon_x \\ \varepsilon_y \\ \gamma_{xy} \end{Bmatrix} = \begin{Bmatrix} \frac{\partial u}{\partial x} \\ \frac{\partial v}{\partial y} \\ \frac{\partial v}{\partial x} + \frac{\partial u}{\partial y} \end{Bmatrix} = \begin{bmatrix} \frac{\partial}{\partial x} & 0 \\ 0 & \frac{\partial}{\partial y} \\ \frac{\partial}{\partial y} & \frac{\partial}{\partial x} \end{bmatrix} \begin{Bmatrix} \mathrm{u} \\ \mathrm{v} \end{Bmatrix} \tag{16}$$

As a result of such strain, stresses build up in a material according to equation 17. Here, it is assumed that the 2D material under consideration is elastic, such that the relation between stresses and strains is linear, and isotropic, such that the constants governing the material properties are the same along all relevant directions [36].

$$\sigma = \mathbf{D}(\boldsymbol{\varepsilon} - \boldsymbol{\varepsilon_0}) + \sigma_\mathbf{0} \tag{17}$$

$\boldsymbol{\varepsilon_0}$ accounts for initial strains resulting from for example crystal growth due to a temperature change or a structural phase transition [34]. $\sigma_\mathbf{0}$ accounts for initial, residual stresses and is often unknown. Moreover, since it is a constant vector we can leave it out of the governing equations.

It is evident that, for there not to be any buildup of stress in a body, $\boldsymbol{\varepsilon} = \boldsymbol{\varepsilon_0}$ should hold. In this case, we can see that the body assumes the displacement field prescribed by the initial strains.

The elasticity matrix $\mathbf{D}$ contains the appropriate material properties and governs the elastic and isotropic behavior of the material. Limiting the analysis to stress in a 2D plane, the elasticity matrix can be derived to be as in equation 18, where E and ν are respectively the Young's modulus and the Poisson's ratio of a material. Here, the fact that the elasticity matrix is symmetric in the x- and y-direction corresponds to the assumption that we are dealing with an isotropic material.

$$D = \frac{E}{1-\nu^2} \begin{bmatrix} 1 & \nu & 0 \\ \nu & 1 & 0 \\ 0 & 0 & \frac{(1-\nu)}{2} \end{bmatrix} \tag{18}$$

In the absence of confinements, such as boundary conditions, non-uniform material properties or discontinuities in the force-field, a body will assume a form corresponding to $\boldsymbol{\varepsilon_0}$, to minimize the present strain. In the presence of one of these factors, the actual form can deviate from this natural shape, causing strain. In general, a material will assume a form as to minimize the potential energy related to the corresponding strain. This potential energy follows from expression 19 [34].

$$\Pi = \frac{1}{2}\int_\Omega \boldsymbol{\varepsilon}^{\boldsymbol{T}}\boldsymbol{\sigma} d\Omega = \frac{1}{2}\int_\Omega \boldsymbol{\varepsilon}^T \mathbf{D}\boldsymbol{\varepsilon} d\Omega - \frac{1}{2}\int_\Omega \boldsymbol{\varepsilon}^T \mathbf{D}\boldsymbol{\varepsilon_0} d\Omega + \frac{1}{2}\int_\Omega \boldsymbol{\varepsilon}^T \boldsymbol{\sigma_0} d\Omega \tag{19}$$

Here, with the eye on allowing for the 'natural' equilibrium dimensions of a material to change, we include an expansion effect. In simple applications modelling thermal expansion, it is assumed that materials stretch linearly with temperature on a certain range. This leads to the thermal expansion coefficients α_x and α_y, which would be equal for isotropic materials, indicating the relative change of size with respect to an equilibrium length L_0 in the respective dimension, per temperature unit [38].

For the modelling objective of the present report, however, we adopt a somewhat alternative interpretation of the expansion coefficients. Namely, we desire to accommodate for the coexistence of two phases with different equilibrium lattice parameters within one material. Now, departing from an equilibrium lattice (say a ferromagnetic state) we can use the coefficients α_x and α_y to model a push towards new lattice parameters in a second phase. Here, the value of α_x corresponds to a relative change in a lattice parameter in line with the x-axis of $100\alpha_x\%$. To model this phase, we use the parameter ϕ. ϕ can assume the values 0 and 1, dependent on the phase. By adopting values for α_y different from α_x, we can not only allow for volume changes, but also for changes of the relative lattice parameters during a phase transition.

$$\boldsymbol{\varepsilon}^{\phi} = \phi \begin{bmatrix} \alpha_x \\ \alpha_y \\ 0 \end{bmatrix} \tag{20}$$

The difference between actual strain and the strain caused by these expansion terms, $\boldsymbol{\varepsilon} - \boldsymbol{\varepsilon}^{\boldsymbol{\phi}}$, leads to the accumulation of stresses inside the body.

5.3 Euler-Lagrange equations

The problem definition as has been developed above and will be developed into a discrete model later in this text, is in the form of a energy-minimization problem. We look for a displacement field such that the potential energy integral in equation 19 is minimized. From this notation,

however, we can also derive a set of corresponding differential equations, the so-called Euler-Lagrange equations, that are equivalent to the energy-minimization notation [35].

Let $(\hat{u}(x,y), \hat{v}(x,y)$ be the energy minimizing displacement field, such that the integral in equation 21 is minimized. For convenience we take a problem in which there is zero displacement at all boundaries and no residual stresses occur in the form of $\boldsymbol{\sigma_0}$

$$\Pi = \frac{1}{2} \int \int \boldsymbol{\varepsilon}^{\boldsymbol{T}} \mathbf{D} \Big(\boldsymbol{\varepsilon} - \phi \begin{bmatrix} \alpha_x \\ \alpha_y \\ 0 \end{bmatrix} \Big) d\Omega \tag{21}$$

We now take a random function $(\eta(x,y), \xi(x,y))$, by which we deviate from the energy-minimizing solution according to equation 22 [35]. Here, γ is a random parameter and the random functions meet the Dirichlet boundary condition. Accordingly, the potential upon plugging this function into equation 21 should be minimal for $\gamma = 0$.

$$\begin{Bmatrix} u(x,y) \\ v(x,y) \end{Bmatrix} = \begin{Bmatrix} \hat{u}(x,y) + \gamma\eta(x,y) \\ \hat{v}(x,y) + \gamma\xi(x,y) \end{Bmatrix} \tag{22}$$

We develop the following integral, which is only a function of γ. Here, $A = \frac{E}{(1-\nu^2)}$ and $B = \frac{E}{2(1+\nu)}$, and the relevant matrix-vector multiplications in equation 21 have been carried out, plugging in the perturbed displacement field in equation 22.

$$\begin{aligned} I(\gamma) = \frac{\partial}{\partial\gamma} \int_\Omega \Bigg(& A\Big(\big(\frac{\partial(\hat{u} + \gamma\eta)}{\partial x} \big) \big(\frac{\partial(\hat{u} + \gamma\eta)}{\partial x} + \nu \frac{\partial(\hat{v} + \gamma\xi)}{\partial y} - \phi\alpha_x - \nu\phi\alpha_y \big) \Big) + \\ & A\Big(\big(\frac{\partial(\hat{v} + \gamma\xi)}{\partial y} \big) \big(\frac{\partial(\hat{v} + \gamma\xi)}{\partial y} + \nu \frac{\partial(\hat{u} + \gamma\eta)}{\partial x} - \phi\alpha_y - \nu\phi\alpha_x \big) \Big) + \\ & B\Big(\frac{\partial(\hat{u} + \gamma\eta)}{\partial y} + \frac{\partial(\hat{v} + \gamma\xi)}{\partial x} \Big)^2 \Bigg) d\Omega \end{aligned} \tag{23}$$

Evaluating this in $\gamma = 0$ and using the fact that only the test functions $\eta(x,y)$ and $\xi(x,y)$ are weighed with γ, we get the following integral.

$$\begin{aligned} I(0) = \int_\Omega \Bigg(& A\Big(2\frac{\partial\eta}{\partial x}\frac{\partial u}{\partial x} + \nu\big(\frac{\partial\eta}{\partial x}\frac{\partial v}{\partial y} + \frac{\partial\xi}{\partial y}\frac{\partial u}{\partial x} \big) - \phi\alpha_x \frac{\partial\eta}{\partial x} - \nu\phi\alpha_y \frac{\partial\eta}{\partial x} \Big) \\ & + A\Big(2\frac{\partial\xi}{\partial y}\frac{\partial v}{\partial y} + \nu\big(\frac{\partial\xi}{\partial y}\frac{\partial u}{\partial x} + \frac{\partial\eta}{\partial x}\frac{\partial v}{\partial y} \big) - \phi\alpha_y \frac{\partial\xi}{\partial y} - \nu\phi\alpha_x \frac{\partial\xi}{\partial y} \Big) \\ & + 2B\Big(\frac{\partial u}{\partial y}\frac{\partial\eta}{\partial y} + \frac{\partial v}{\partial x}\frac{\partial\xi}{\partial x} + \frac{\partial\eta}{\partial y}\frac{\partial v}{\partial x} + \frac{\partial\xi}{\partial x}\frac{\partial u}{\partial y} \Big) \Bigg) d\Omega \end{aligned} \tag{24}$$

Now, upon integration by parts, where we use the fact that the test functions are sufficiently smooth and equal to zero at the boundary, we obtain the integral 25.

$$I(0) = -\int_\Omega \Bigg(A\Big(2\eta\frac{\partial^2 u}{\partial x^2} + 2\nu\eta\frac{\partial^2 v}{\partial x\partial y} + 2\nu\xi\frac{\partial^2 u}{\partial x\partial y} + 2\xi\frac{\partial^2 v}{\partial y^2}\Big) + \\ 2B\Big(\eta\frac{\partial^2 u}{\partial y^2} + \xi\frac{\partial^2 v}{\partial x^2} + \eta\frac{\partial^2 v}{\partial x\partial y} + \xi\frac{\partial^2 u}{\partial x\partial y}\Big) \\ -\Big(\eta(\nu\alpha_y + \alpha_x)\frac{\partial\phi}{\partial x} + \xi(\nu\alpha_x + \alpha_y)\frac{\partial\phi}{\partial y}\Big)\Bigg) d\Omega \tag{25}$$

Now, using the fact that $\eta(x, y)$ and $\xi(x, y)$ are independent, random functions, in order for $I(0) = 0$ to hold, the following equations must hold.

$$A\frac{\partial^2 u}{\partial x^2} + A\nu\frac{\partial^2 v}{\partial x\partial y} + B\frac{\partial^2 u}{\partial y^2} + B\frac{\partial^2 v}{\partial x\partial y} - \frac{1}{2}(\nu\alpha_y + \alpha_x)\frac{\partial\phi}{\partial x} = 0 \tag{26}$$

$$A\frac{\partial^2 v}{\partial y^2} + A\nu\frac{\partial^2 u}{\partial x\partial y} + B\frac{\partial^2 v}{\partial x^2} + B\frac{\partial^2 u}{\partial x\partial y} - \frac{1}{2}(\nu\alpha_x + \alpha_y)\frac{\partial\phi}{\partial y} = 0 \tag{27}$$

Relating this back to the stress and strain tensors as defined before, we find the following differential equations to be equivalent to the minimization problem as defined in integral form. Here, $\boldsymbol{\sigma} = \begin{Bmatrix} \sigma_{xx} \\ \sigma_{yy} \\ \tau_{xy} \end{Bmatrix}$

$$\frac{\partial}{\partial x}\sigma_{xx} + \frac{\partial}{\partial y}\tau_{xy} - \frac{1}{2}(\nu\alpha_y + \alpha_x)\frac{\partial\phi}{\partial x} = 0 \tag{28}$$

$$\frac{\partial}{\partial y}\sigma_{yy} + \frac{\partial}{\partial x}\tau_{xy} - \frac{1}{2}(\nu\alpha_x + \alpha_y)\frac{\partial\phi}{\partial y} = 0 \tag{29}$$

The Euler-Lagrange equations contain the partial derivatives of the phase-parameter ϕ. However, since this is a discrete variable that takes either the value 0 or 1, such a derivative is ill-defined at boundaries between the two different phases. Since in the phase-field we deal with step-functions between the different phases, the partial derivatives of this field translate into a delta-forcing at the phase-boundaries. This discontinuity can be expected to influence the convergence of the FEM and requires further study.

5.4 Discretization

The discretization of any problem subject to FEM occurs through the subdivision of a certain domain into elements [34]. Accordingly, the continuous solution to the relevant problem is approximated by plugging the discretized version of a continuous field into the respective funtional. In this thesis, discretization of 2D-space occurs into triangular elements, for reasons that will become evident later. Each element has three nodes, as depicted in figure 14. Now, the deformation of the body, which is a continuous function of the equilibrium positions, is discretized by considering only the displacements of the nodes of the triangle elements. For each coordinate in an element, we seek an approximation of its displacement as a linear combination of the nodal point displacements.

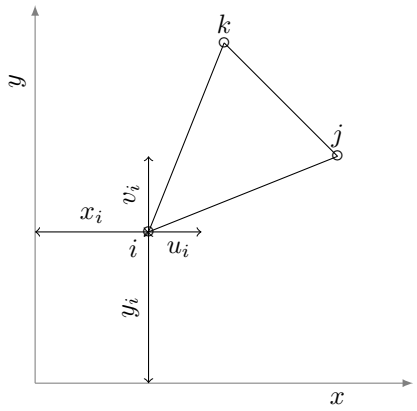

Figure 14: A triangle element with three nodes indexed by i,j, and k. The nodal points have a starting position (x_p,y_p) and displacement (u_p,v_p), with p the relevant index, as indicated for nodal point i.

$$u(x,y) = N_i(x,y)u_i + N_j(x,y)u_j + N_k(x,y)u_k \tag{30}$$

$$v(x,y) = N_i(x,y)v_i + N_j(x,y)v_j + N_k(x,y)v_k \tag{31}$$

Here, $N_i(x,y)$ should evidently be equal to 1 at node i, whereas N_j and N_k are equal to 0 at this node [34]. The same holds, mutatis mutandis, under rotation over the indices.

It can be shown that the system of equations corresponding to these linearizing functions and the respective conditions on the nodal values is solved by the following result [37].

$$N_i = \frac{a_i + b_i x + c_i y}{2A} \tag{32}$$

with

$$a_i = x_j y_m - x_m y_j \tag{33}$$

$$b_i = y_j - y_m \tag{34}$$

$$c_i = x_m - y_J \tag{35}$$

With A the area of the triangle element, given by

$$A = \frac{1}{2}\det \begin{bmatrix} 1 & x_i & y_i \\ 1 & x_j & y_j \\ 1 & x_k & y_k \end{bmatrix} \tag{36}$$

N_j and N_k and the respective coefficients follow under rotation over the indices. Accordingly, we derive the following linearization of the displacement at an initial position (x,y) in an element [37].

$$\begin{Bmatrix} \mathrm{u(x,y)} \\ \mathrm{v(x,y)} \end{Bmatrix} \approx \begin{bmatrix} N_i & 0 & N_j & 0 & N_k & 0 \\ 0 & N_i & 0 & N_j & 0 & N_k \end{bmatrix} \begin{Bmatrix} \mathrm{u}_i \\ \mathrm{v}_i \\ \mathrm{u}_j \\ \mathrm{v}_j \\ \mathrm{u}_k \\ \mathrm{v}_k \end{Bmatrix} = \mathbf{Nd} \tag{37}$$

Here, $\mathbf{d}$ is the displacement vector of the element's nodes. Now, recalling the strain tensor, we can derive a discretization of the strain in an element as well.

$$\boldsymbol{\varepsilon} = \begin{bmatrix} \frac{\partial}{\partial x} & 0 \\ 0 & \frac{\partial}{\partial y} \\ \frac{\partial}{\partial y} & \frac{\partial}{\partial x} \end{bmatrix} \begin{Bmatrix} \mathrm{u} \\ \mathrm{v} \end{Bmatrix} \approx \mathbf{Bd} \tag{38}$$

Here, $\mathbf{B}$ is the matrix resulting from taking the respective derivatives. In the case of triangular elements this is, conveniently, a matrix containing only constants [37].

$$\mathbf{B} = \frac{1}{2A} \begin{bmatrix} b_1 & 0 & b_2 & 0 & b_3 & 0 \\ 0 & c_1 & 0 & c_2 & 0 & c_3 \\ c_1 & b_1 & c_2 & b_2 & c_3 & b_3 \end{bmatrix} \tag{39}$$

We are now ready to discretize a stress-strain problem. Only dealing with the effect of phase-transitions, through the use of the coefficients α_x and α_y we consider a situation without body- and tensile forces. It is the objective to minimize the potential energy, given as

$$\Pi = \frac{1}{2} \int \boldsymbol{\varepsilon}^{\boldsymbol{T}} \boldsymbol{\sigma} dV \tag{40}$$

Dividing the volume V into disjoint elements, this integral can be represented as follows.

$$\Pi = \frac{1}{2} \sum_{elts} \int_{V_e} \boldsymbol{\varepsilon}^{\boldsymbol{T}} \boldsymbol{\sigma} dV \tag{41}$$

We now recall the relation $\sigma = \mathbf{D}\boldsymbol{\varepsilon}$ and assume that a single element is in one or the other phase (thus $\phi = 0$ or $\phi = 1$ throughout the element). Upon the linearization of strain $\boldsymbol{\varepsilon}$ according to equation 38 we derive the product of matrices that are constant throughout an element. Accordingly, the integration simply results in a prefactor of tA_e, where t is the element's thickness (assumed to be the same for all elements), and A_e its surface. The following approximation of the bodies potential results:

$$\Pi \approx \frac{1}{2} t \sum_{elts} A_e (\mathbf{Bd})^T \mathbf{D} (\mathbf{Bd} - \phi \begin{bmatrix} \alpha_x \\ \alpha_y \\ 0 \end{bmatrix}) \tag{42}$$

Now the displacement of the nodal points are the remaining variables. Given a phase-field, the derivatives of equation 42 are taken with respect to the nodal displacements. The result is a system of linear equations, the solution to which gives us the nodal displacements that approximate the energy- minimizing displacement field corresponding to this phase-field.

5.5 Meshing

Given a domain and a mathematical problem subjected to the FEM, the discretization of this domain permits for a lot of freedom regarding the meshing, the selection of nodal points and subsequent definition of elements, of this domain. The reader is reminded of the fact that the objective of the present work is to relate the degree of porosity in a domain to the build-up of stresses in this domain. Accordingly, the selected meshing approach should provide us with the possibility to introduce voids into the interior of the domain. In the present work, two different approaches to this meshing have been implemented. In both implementations, a $200\mu\mathrm{m} \times 200\mu\mathrm{m}$ domain has been subdivided into square-shaped subdomains with the dimensions $20\mu\mathrm{m} \times 20\mu\mathrm{m}$.

Each subdomain represents a physical element that undergoes a phase transition as a whole, an will be referred to as a *grain* in the remainder of this text. It should be noted that the absolute values of the dimensions of these grains do not influence the values of the resulting stresses.

Firstly, a grid has been developed in which the dimensions of the elements were predetermined. Here, the point of departure is a rectangular domain, subdivided into rectangles (two triangular elements), all with the same dimensions. See figure 15a for an example of this grid. In this approach, two triangles forming a rectangle were interpreted as a grain. The thought behind this predetermined meshing was to reduce the effect of element shapes on the development of stresses in an element. If all elements have the same dimensions, we should expect the effect the dimensions of an element have on the behavior of this element to be the same for all elements.

This mesh has subsequently been adapted in order to allow for the periodic insertion of voids into the interior of the domain. See figure 15b for an example of this grid. In this mesh, every element is incident with at least one node on a void. The ratio behind this is that, when a node is incident on a porous spot in stead of being shared by one or two elements more, it has more freedom to adjust and be displaced in a direction corresponding to the phases of the elements that are still incident on this node. A consequence of this meshing, however, is that we depart from a grid with elements that all have the same starting dimensions and introduce, next to square-shaped grains, rectangular grains. In the limit of low levels of porosity, the ratio between the height and base of these elements gets very big. Since this is reported to influence the accuracy of the computed forces due to increasing interpolation errors, we should be wary of this effect [39].

Secondly, the PDE Toolbox environment in MATLAB has been used to perform the meshing. In this environment, one can define the boundaries of a domain, after which this domain is subjected to the delaunay triangulation algorithm [40][41]. An example of this triangulation is presented in figure 15c. In order to have some resemblance to the first meshing approach and the respective subdivision of the elements into grains, we can now select elements based on their position in one or the other rectangular subdomain and distribute the elements over grains accordingly. However, there is no full control over for example the orientation of the boundaries of the respective grains in this case.

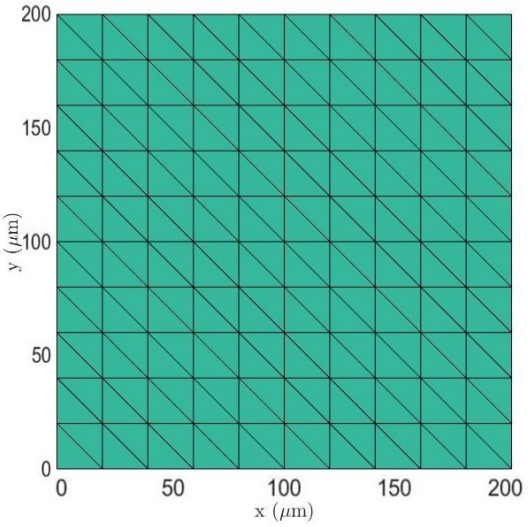

(a) Grid type 1, regular

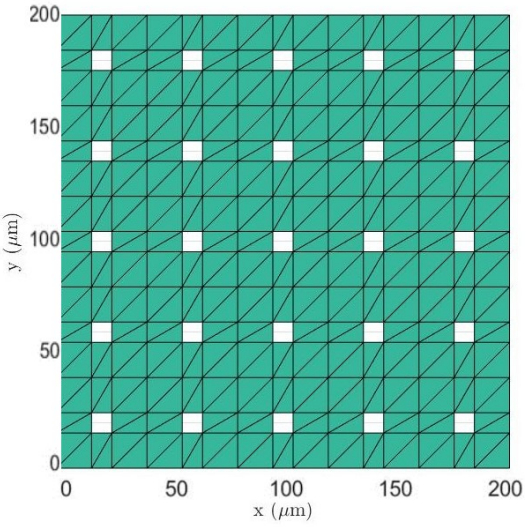

(b) Grid type 1, 5% porosity

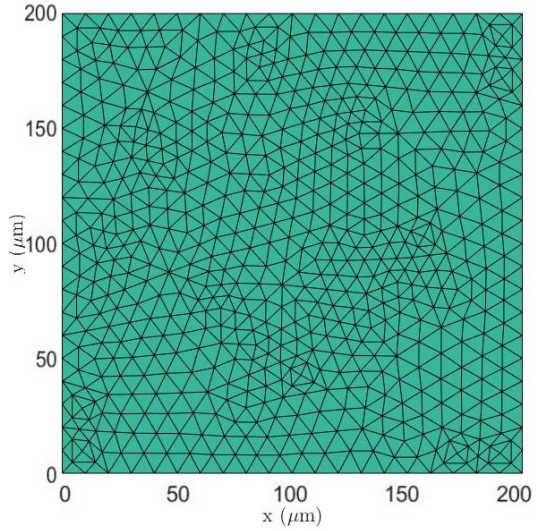

(c) Grid type 2, regular

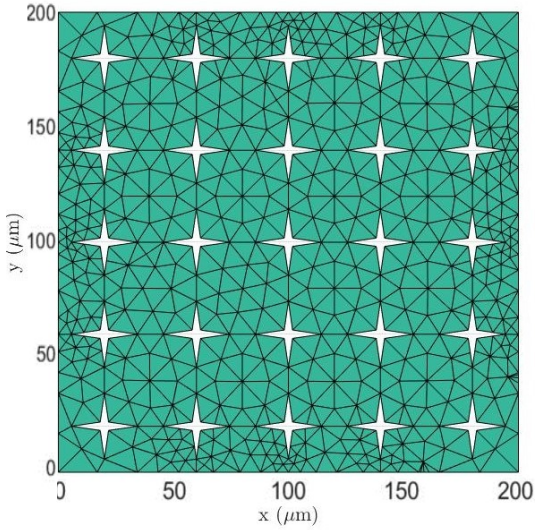

(d) Grid type 2, 5% porosity

Figure 15: Exemplary grids, regular and porous, of type 1 and 2. Grid type 2 allows for more freedom regarding the shapes of voids to be included into the domain. The downside of this method is the reduced control one has over the number, distribution, and size of the triangular elements.

Porosity is introduced into this grid by defining internal boundaries and meshing the remaining parts of the domain. Here, there is quite some freedom regarding the types of shapes the PDE Toolbox allows to define, namely squares, ellipses, and polynomials. An example of the latter grid is presented in figure 15d. Since this shape-type seems to most closely resemble the shape of voids in actual materials (see [20] for an example), it is used in the present work. Here, it is evident that at the internal boundaries, the triangulation algorithm leads to a a finer mesh in order to fill up the space around sharp corners with elements. Accordingly, we loose control over the size and dimensions of the elements in a mesh, which is a point of attention in the analysis of results.

5.6 Forces and fractures

The objective of this part of the present thesis is to model the development of stresses during the passing of a simple 2D model through a magnetostructural transition. Accordingly, we shall define the stresses that build up in the respective material.

The reader is reminded of the stress tensor as defined above.

$$\sigma = \mathbf{D}(\varepsilon - \phi \begin{bmatrix} \alpha_x \\ \alpha_y \\ 0 \end{bmatrix}) \tag{43}$$

Such that

$$\sigma_{xx} = \frac{E}{1-\nu^2}(\frac{\partial u}{\partial x} + \nu\frac{\partial v}{\partial y} - \phi\alpha_x - \nu\phi\alpha_y) \tag{44}$$

$$\sigma_{yy} = \frac{E}{1-\nu^2}(\frac{\partial v}{\partial y} + \nu\frac{\partial u}{\partial x} - \phi\alpha_y - \nu\phi\alpha_x) \tag{45}$$

$$\tau_{xy} = \frac{E}{2(1+\nu)}(\frac{\partial u}{\partial y} + \frac{\partial v}{\partial x}) \tag{46}$$

Here, σ_{xx} and σ_{yy} are normal/tensile stresses in respectively the x- and y- direction, accounting for deformations that retain a rectangular structure. See figure 16a for an example. τ_{xy} is the shear stress. A non-zero value for this component corresponds to deviations from the rectangular geometry that is used in this thesis, so-called shearing, as is displayed in figure 16b. All of these forces, which consist of derivatives of the linearizations of displacement in an element, have a constant value throughout a triangular element in the FEM. Due to the coexistence of phases, we should expect stresses to develop in a material as grains are confined in assuming the equilibrium dimensions corresponding to their respective phase. This follows from the Euler-Lagrange equations corresponding to this model as derived above, as a discontinuity in the phase-field leads to a delta-peak force at the place of this discontinuity. Accordingly, in the present thesis, the behavior of $\|\boldsymbol{\sigma}\|$ will be considered, mostly as a check as to whether or not the development of this variable follows our expectations. In the remainder of this text, for the tensors $\boldsymbol{\sigma}$ and $\boldsymbol{\varepsilon}$ the conventional norm notation $\|\cdot\|$ refers to the Frobenius norm, the logical extension of the Euclidean norm as defined for vectors towards tensors and matrices [42].

The formation and propagation of fractures in a material, however, mostly occur at grain boundaries [20][43]. Here, the expected result is that fracturing occurs at the interface between the two phases in our model. Considering an edge that is shared by two elements, a jump in the shear stress from one of the elements incident on this edge to the other translates into a pull exerted on this edge, as is displayed in figure 16c. Such a jump could lead to the initiation of a crack.

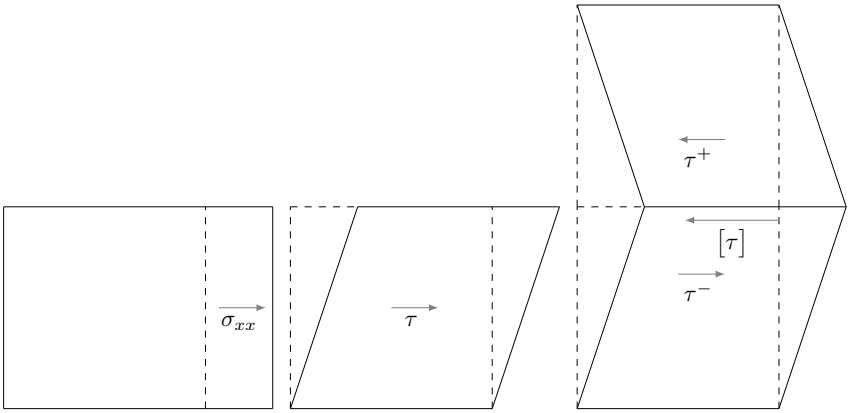

Figure 16: Stresses caused by the deviation of a tetragonal element (full lines) from its square shape that would be assumed in the absence of confinements (dotted lines). (a) Tensile stress along the x-direction (b) Shear stress, for convenience illustrated with only $\frac{\partial u}{\partial y}$ nonzero (c) Jump in shear stress at a shared edge.

Now, in order to properly compute the value of this jump in shear stresses across and edge, $[\tau]$, we should process the orientation of the respective edge. Let θ be the angle of an edge with respect to the x-axis. In order to consider the transformation of stresses in a point to the new coordinate system associated with this angle, we consider a infinitesimal area dA at an angle θ with the y-axis, as presented in figure 17b [44].

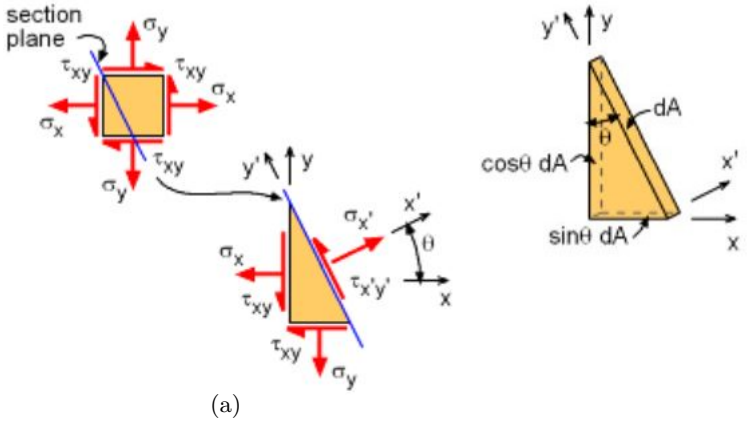

Figure 17: (a) Stresses in a coordinate system corresponding to a section plane with an angle θ due to counterclockwise rotation. (b) Infinitesimal surface element. Figures due to [45]

Now, if the element is in a static equilibrium, all forces acting on the section plane should be in balance with the forces acting on the outside surfaces. Accordingly,

$$\sum F_x = (\sigma_{x'x'}dA)\cos\theta - (\tau_{x'y'}dA)\sin\theta - \sigma_{xx}(\cos\theta dA) - \tau_{xy}(\sin\theta dA) \tag{47}$$

and

$$\sum F_y = (\sigma_{x'x'} dA) \sin\theta - (\tau_{x'y'} dA) \cos\theta - \sigma_{yy}(\sin\theta dA) - \tau_{xy}(\cos\theta dA) \tag{48}$$

Here, no $\sigma_{y'y'}$ appears since the respective direction is parallel to the section plane. Solving for the two unknowns $\sigma_{x'x'}$ and $\tau_{x'y'}$, the latter follows from equation 49 [44].

$$\tau'_{xy} = (\sigma_{yy} - \sigma_{xx}) \sin\theta \cos\theta + \tau_{xy}(cos^2\theta - sin^2\theta) \tag{49}$$

For an edge with two incident elements and respective shearing stresses τ^+ and τ^- computed according to equation 49, the jump in shear stress follows from equation 50.

$$\left[\tau\right] = |\tau^+ - \tau^-| \tag{50}$$

The θ-dependence of the shear stress and accordingly of $\left[\tau\right]$ implies that the triangulation of our domain and the respective edge-orientations will likely influence the distributions of $\left[\tau\right]$.

5.7 Analysis

After the implementation of the model in line with what has been presented in the preceding paragraphs, a magnetic phase transition is simulated as follows. In both grid types, we identify physical elements, grains, that are defined to always occur in the same phase. For grid type 1, this is simply the rectangle formed by two neighboring triangular elements. In grid type 2, the domain is divided into square-shaped grains. The elements are grouped into a subdomain according to the location of their centre of mass.

At each discrete step of the transition, all grains that have not passed through the transition have a transition probability, which is the same for all groups and at every step. From this stochastic, step-by-step passing through a transition, we acquire a distribution of the elements over $\phi = 0$ and $\phi = 1$ at each step of a transition simulation. This process is repeated several times and the respective results aggregated. Accordingly, the cyclic passing through a magnetostructural transition by a substrate is simulated. The parameter values as used throughout these simulations are as presented in table 6. The boundary conditions used in this work are as follows: of the element incident on the bottom left corner one node is fixed at (0μm, 0μm) and the other two nodes are fixed on the axis on which they are respectively placed.

Table 6: Parameter values used throughout the simulated phase transitions in the remainder of this work.

Variable	E	ν	α_x	α_y	Steps per transition	Transition probability
Value	100 GPa	$\frac{1}{3}$	0.01	-0.01	8	25%

6 Results

In the present section, the results of the implementation of the FEM model as discussed in the previous section are discussed. Firstly, attention is paid to the convergence of various parameters in the respective model. Secondly, the functioning of the model on grid type 1 is evaluated. Lastly, the model is evaluated on grid type 2, leading into a more thorough analysis of the results on the respective grid.

6.1 Convergence

As has been noted after derivation of the Euler-Lagrance equations corresponding to our energy-minimization problem, the discontinuity of the phase-field can be expected to reduce the convergence rate of the corresponding FEM-model. Accordingly, the convergence of the developed model has been studied for a sample phase-field.

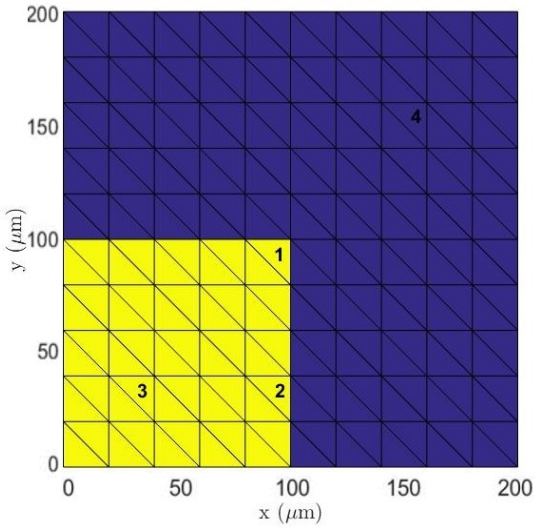

Figure 18: phase-field to which the substrate was subjected in order to test for the convergence of $\|\mathbf{u_h}\|$, $\|\boldsymbol{\varepsilon_h}\|$, and $\|\boldsymbol{\sigma_h}\|$ at points 1,2,3, and 4. $\phi = 1$ in the yellow elements, $\phi = 0$ in the blue elements. For $\|\boldsymbol{\varepsilon_h}\|$, the displacement of the respective top right node for each element has been used.

Let us assume that some metric x_h in an FEM-model converges to a value C corresponding to the exact solution upon refinement of the grid to infinitesimal elements. Thus,

$$\lim_{h \to 0} x_h = C \tag{51}$$

If we now assume that the error in x_h scales with h^p, with p an integer, we can estimate the value of p as follows. Here, $C(h)$ denotes the value of the respective metric under a grid with element width h and k is a constant and unknown parameter that is equal across the estimations.

$$\begin{aligned} C(h) &= C + kh^p + 0(h^{p+1}) \\ C(2h) &= C + k(2h)^p + 0(h^{p+1}) \\ C(4h) &= C + k(4h)^p + 0(h^{p+1}) \end{aligned} \tag{52}$$

Simple algebraic manipulations, neglecting the higher order error terms, lead to the following expression for 2^p.

$$2^p = \frac{C(4h) - C(2h)}{C(2h) - C(h)} \tag{53}$$

Applying this method to the phase-field in figure 18 and the values of of $\|\mathbf{u_h}\|$, $\|\boldsymbol{\varepsilon_h}\|$, and $\|\boldsymbol{\sigma_h}\|$ at points 1,2,3, and 4, we get the convergence orders as presented in 7.

Table 7: Convergence orders according to formula 53 and the phase-field in figure 18

Position \ Metric	$\|\mathbf{u_h}\|$	$\|\boldsymbol{\varepsilon_h}\|$	$\|\boldsymbol{\sigma_h}\|$
1	1.99	-0.16	-0.02
2	2.04	1.13	0.76
3	1.70	0.90	0.84
4	2.01	1.06	1.04

Firstly, let us note that with respect to the displacement, the method appears to be of order 2, as the FEM is reported to be for well defined problems. This holds irrespective of the type of node under consideration (in the bulk of a phase, at a one-fold or two-fold interface between the two faces). Accordingly, the discontinuity in the phase-field does not seem to influence this metric.

If we consider the orders of convergence of $\|\boldsymbol{\varepsilon_h}\|$ and $\|\boldsymbol{\sigma_h}\|$, however, the observations are not similar over the different types of points. Firstly, since these two metrics are derived as derivatives of the displacement field, the expectation is that the order with respect to these metrics is one lower than the order with respect to the displacement. This appears to hold for both positions 3 and 4, which are located in the bulk of a phase, and for position 2, which is located at a onefold phase-interface. For all these points, the approximate orders are closest to the integer 1. However, for position 1, located at a corner or twofold phase-interface, the order for $\|\boldsymbol{\varepsilon_h}\|$ and $\|\boldsymbol{\sigma_h}\|$ is close to zero. In other words, there is no convergence to some fixed value upon refinement of the grid into infinitesimal elements. Accordingly, the respective metrics should tend to infinity upon refinement of the grid.

The implications of this finding to the continuation of this report are as follows. Firstly, we expect extremes in the values for $\boldsymbol{\sigma}$ inside elements and $\left[\tau\right]$, which derives from the differences of the components of $\boldsymbol{\sigma}$ between two elements across an edge, to reach extremes at the interface between phases. Accordingly, the fact that these values likely do not converge at such points should be taken into consideration. Secondly, the assumptions of continuum mechanics regarding for example elastic behavior do not hold at the atomic level [46]. Accordingly, refinement of a grid to infinitesimal dimensions is not only computationally impossible, it also violates the assumptions laying at the core of the present modelling endeavour. Therefore, we should take the prediction of forces rising to infinite values with a grain of salt.

6.2 Grid Type 1

In the present section, the behavior of the model on grid type 1 is discussed. Firstly, some figures indicating the positions of the maximum values of $\|\boldsymbol{\sigma}\|$ and $\lceil\tau\rceil$ in a given phase-field are presented to illustrate the trends in these occurrences. Hereafter, the distribution of $\lceil\tau\rceil$ is manipulated into a metric that serves to have a base check as to whether or not the model meets a basic set of expectations on the respective grid.

In figure 19, a sample is presented of the elements and nodes with the position of the highest values of respectively $\|\boldsymbol{\sigma}\|$ and $\lceil\tau\rceil$ (as defined in section 5.6) from several simulations with the parameter values as presented in table 6. Of course, many more figures have been analyzed, and this selection has been found to be representative of the trends observed in this bigger sample.

In general, $\|\boldsymbol{\sigma}\|$ has extreme values at the interface between the two phases, as was to be expected. However, the behavior of $\lceil\tau\rceil$ shows an odd deviation from the stated expectation that the discontinuity in the shear stress at an edge would be greatest if this edge were to be located at a phase interface. The maximum values do tend to lay close to an interface between phases, for example where an isolated grain is in in different phase than its direct neighbors. However, here the edge with a maximum value for $\lceil\tau\rceil$ is not identified to be one of the horizontally or vertically oriented edges that have been modelled as grain boundaries, but the diagonal of such a grain, which is per definition sandwiched between two triangles in the same phase.

The above observations suggest that the model as implemented on grid type 1 provides some of the basic mechanisms as expected, such as the location of maximum values of $\|\boldsymbol{\sigma}\|$, but that the orientation of edges likely influences the development of $\lceil\tau\rceil$ in a way that violates the expectations imposed on this model.

A same analysis was performed of the occurrence of maximum values for $\|\boldsymbol{\sigma}\|$ and $\lceil\tau\rceil$ on a porous grid with 11% porosity, corresponding to the regular grid with every 9^{th} grain replaced by a void. A selection of representative occurrences these extremes is presented in figure 20. Here, the observations are not much different, in that both $\|\boldsymbol{\sigma}\|$ and $\lceil\tau\rceil$ are drawn towards phase interfaces, but that $\lceil\tau\rceil$ is positioned at a nearby diagonal edge in stead of at a grain boundary.

To corroborate the observation that the behavior of $\lceil\tau\rceil$ does not meet our basic expectations, a quantitative measure was developed. For each phase-field the edges have been subdivided as follows. For edges shared by two elements, the state of the two incident elements in a given phase-field is compared through the binary variable $\Delta\phi$. If these elements share the same value for ϕ, the respective edge is attributed a value of 0. If the states of the incident elements differ, the edge is attributed a value of 1. The edges that are incident on only element are left out of consideration, since here there is no phase difference to be defined over these edges. Subsequently, the values of $\lceil\tau\rceil$ for the first group of edges has been subjected to a linear regression on the binary variable $\Delta\phi$. Based on the argument that $\lceil\tau\rceil$ is expected to be higher for edges at a phase-interface, the value of the resulting regression coefficient should be positive. If this does not hold, then this is an indication that the model on the respective mesh does not properly simulate the basic physical mechanisms that it is ought to model for.

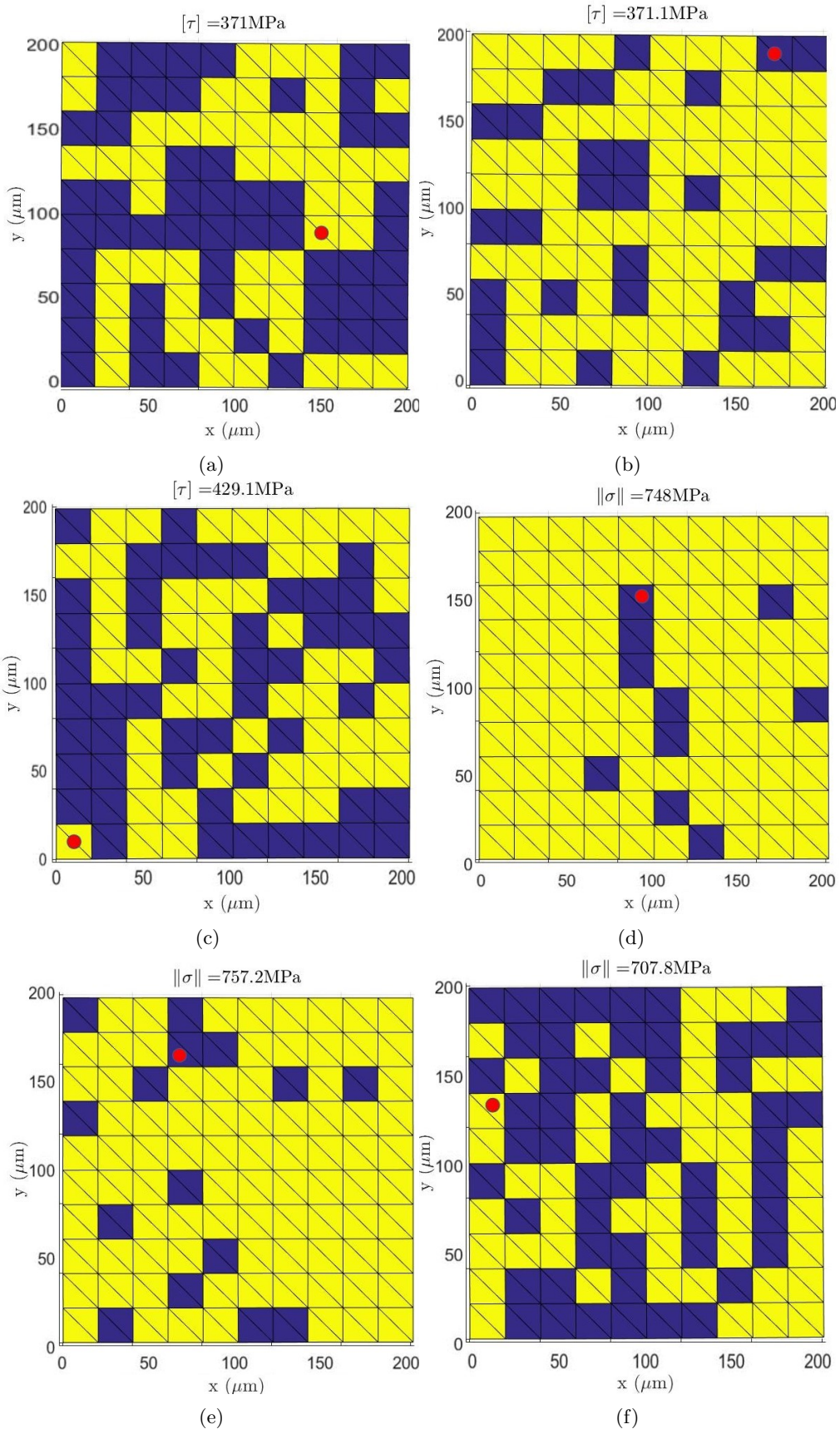

Figure 19: A sample of the phase-fields corresponding to the maximum values of, in figures (a) to (c), $[\tau]$ and, in figures (d) to (f), $\|\boldsymbol{\sigma}\|$. The elements, respectively edges, corresponding to these maximum values are marked by a red dot. Extremes seem to occur most often near interfaces between the two phases. However, the maximums in $[\tau]$ are drawn towards the diagonal inside the grains near such phase interfaces.

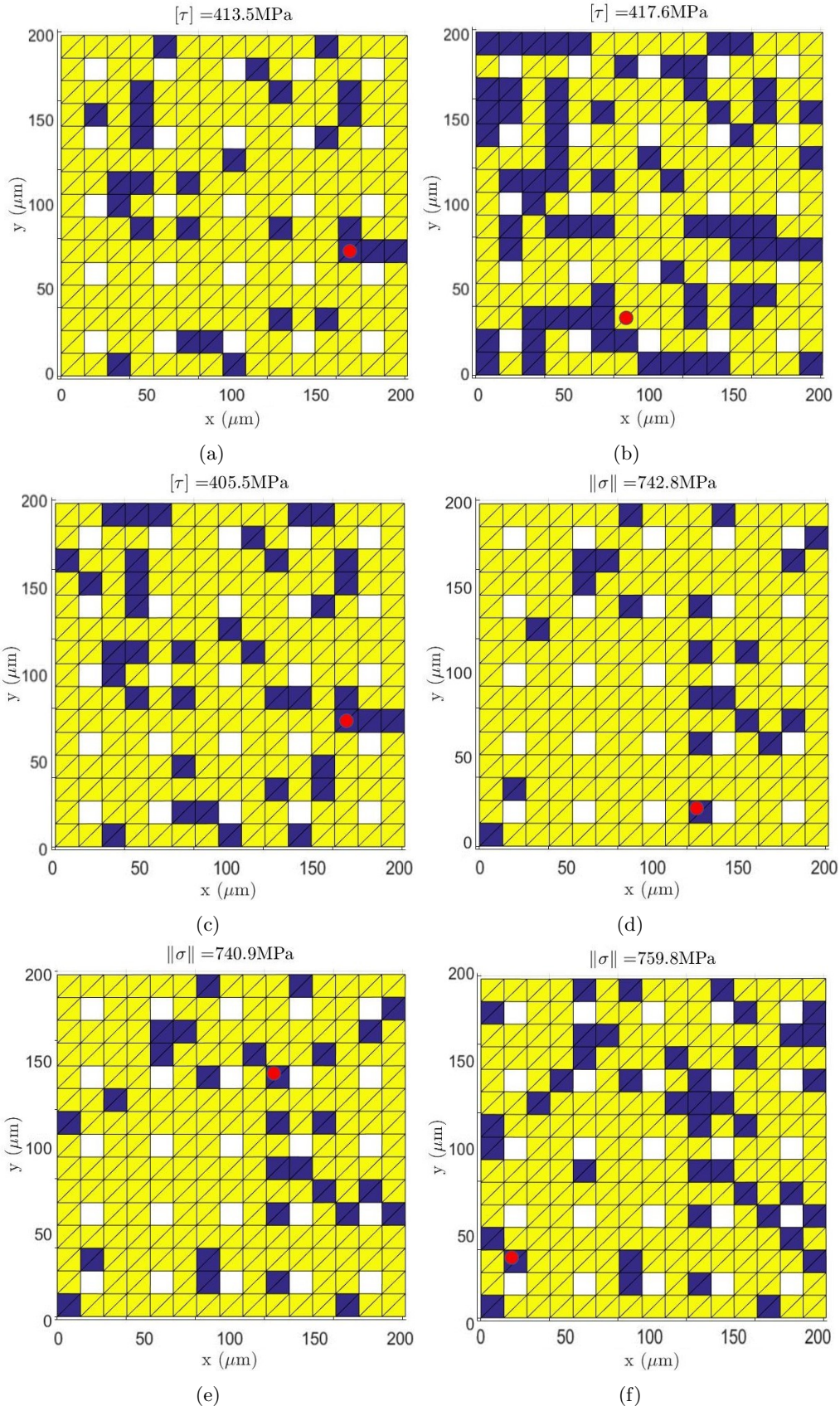

Figure 20: A sample of the phase-fields corresponding to the maximum values of, in figures (a) to (c), $[\tau]$ and, in figures (d) to (f), $\|\boldsymbol{\sigma}\|$ on grid with 11% porosity. The elements, respectively edges, corresponding to these maximum values are marked by a red dot. Here as well, the maximum values in $[\tau]$ are drawn towards the diagonal inside the grains near such phase interfaces.

Table 8: Coefficients corresponding to the linear regression of the values for $\lfloor\tau\rfloor$ of edges located in the bulk of the grid (incident on two elements) and the binary variable $\Delta\phi$ accounting for a phase difference between the two incident elements. $\lfloor\tau\rfloor = \alpha\Delta\phi + \beta$

Grid	α	β
Regular	$(1.9 \pm 0.1) \cdot 10^7$	$(8.36 \pm 0.06) \cdot 10^7$
11%	$(-1.04 \pm 0.08) \cdot 10^7$	$(8.34 \pm 0.04) \cdot 10^7$
5%	$(-4.8 \pm 0.9) \cdot 10^6$	$(8.11 \pm 0.01) \cdot 10^7$
2%	$(3 \pm 1) \cdot 10^6$	$(9.44 \pm 0.05) \cdot 10^7$
1%	$(-5 \pm 1) \cdot 10^6$	$(1.07 \pm 0.01) \cdot 10^8$

The respective coefficients are presented for the regular grid and the porous grid with varying levels of porosity in table 8. In all cases, the coefficient α, accounting for the effect of a phase difference over an edge and the value for $\lfloor\tau\rfloor$ over this edge, is either negative or just weakly positive. This corresponds to what has been stated based on the samples of positions of maximum values of $\lfloor\tau\rfloor$ provided in figures 19 and 20. Moreover, the coefficient β indicates that the introduction of porosity does not lead to a reduction in the average values of $\lfloor\tau\rfloor$.

Accordingly, the limitations of the grid type as as developed here become evident. Firstly, it does not simulate a basic set of physical principles that we expect to be met, such as the appearance of higher shear forces discontinuities across edges located between two phases than on those in the bulk of a phase. This seems to be the consequence of the division of edges into two categories: those vertically or horizontally oriented and accordingly identified as grain boundaries, and those diagonally oriented in a grain. The orientation of an edge seems to outweigh the effect of being located at a phase interface. Secondly, a big limitation of the grid developed here is that it does not allow for grid refinement, such that no tests can be developed as to get to the cause of the strange behavior of $\lfloor\tau\rfloor$. In a finer mesh, we would have a bigger diversity of edge types (near a phase-interface or in the bulk of the material) and could accordingly identify correlations between the edge type and the development of stresses at such an edge. On these grounds, we reject grid type 1 and proceed with grid type 2, which allows for more freedom in the grid definition.

6.3 Grid Type 2

In the preceding subsection it has been found that grid type 1 and the respective implementation of porosity lead to results that go against the basic expectations that our modelling endeavour is ought to meet. Accordingly, a second approach to meshing and subsequently introducing porosity into a domain has been implemented. The fundamental difference between these models is that the symmetry in the mesh is lost, as well as the control over for example element size and shape. This method, however, allows for remeshing and can accordingly come in handy to provide more insight into the relation between the distance of an element or edge to voids in a domain and the development of $\|\boldsymbol{\sigma}\|$ and $\lceil\tau\rceil$, respectively.

6.3.1 Model evaluation

Firstly, the maximum values of $\|\boldsymbol{\sigma}\|$ and $\lceil\tau\rceil$ over several runs for a regular grid with no porosity and a porous grid were considered to identify consistencies in the location of these maximums. Here, the star-shaped voids in the porous grid are positioned in such a way as to partially cover the boundary between neighboring phase-groups. Moreover, in order to also admit for phase interfaces that are not touched upon by a void, the voids have been positioned in an alternating fashion.

A sample of phase-fields with the positions with maximum values for $\|\boldsymbol{\sigma}\|$ and $\lceil\tau\rceil$ is presented in figures 21 and 22. Maximum values in $\|\boldsymbol{\sigma}\|$ and $\lceil\tau\rceil$ in the regular grid have been observed to consistently occur at the interface between two different phases. In the case of the porous grid, the maximums are also located at phase interfaces.

As has been done for grid type 1, the values of $\lceil\tau\rceil$ over an edge located in the bulk of the substrate was regressed on the phase difference $\Delta\phi$ between the two elements incident on this edge. In table 9, the respective coefficients are presented for the regular grid and the porous grid in figures 21 and 22. Here, the strong positive correlation between the occurrence of a phase difference across an edge and the value of $\lceil\tau\rceil$ over this edge holds for both structures, as is physically expected. Accordingly, we have reason to continue with the present model.

Table 9: Coefficients corresponding to the linear regression of the values for $\lceil\tau\rceil$ of edges located in the bulk of the grid (incident on two elements) and the binary variable $\Delta\phi$ accounting for a phase difference between the two incident elements. $\lceil\tau\rceil = \alpha\Delta\phi + \beta$

Grid	α	β
Regular	$(2.85 \pm 0.02) \cdot 10^8$	$(4.88 \pm 0.03) \cdot 10^7$
Porous	$(2.89 \pm 0.01) \cdot 10^8$	$(3.47 \pm 0.01) \cdot 10^7$

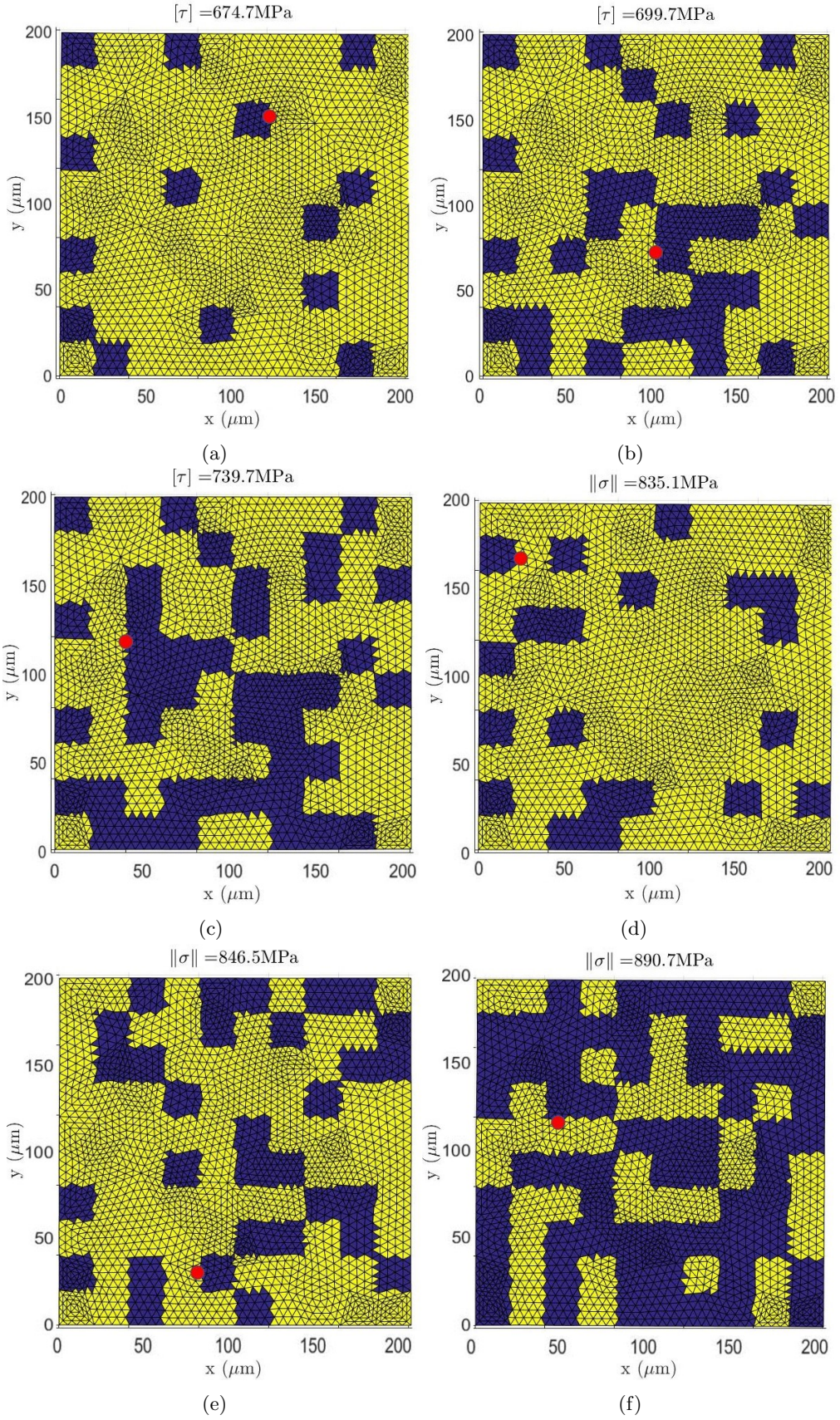

Figure 21: A sample of the phase-fields corresponding to the maximum values of, in figures (a) to (c), $[\tau]$ and, in figures (d) to (f), $\|\boldsymbol{\sigma}\|$ as observed during 10 simulated phase transitions on a regular grid of type 2. The edges, respectively elements, corresponding to these maximum values are marked by a red dot. Extremes occur most often at interfaces between the two phases.

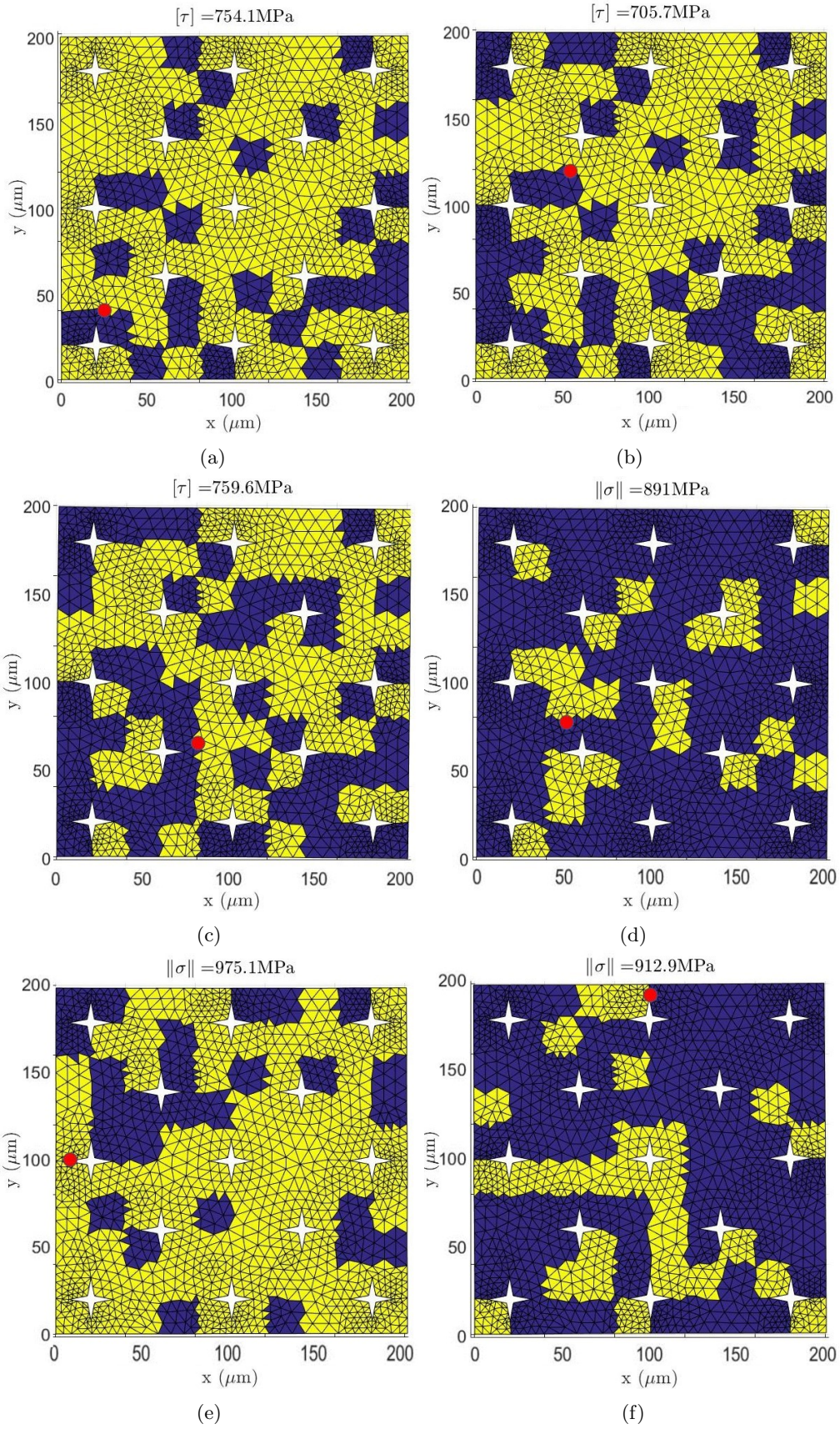

Figure 22: A sample of the phase-fields corresponding to the maximum values of, in figures (a) to (c), $[\tau]$ and, in figures (d) to (f), $\|\boldsymbol{\sigma}\|$. The edges, respectively elements, corresponding to these maximum values are marked by a red dot. The extremes in both $[\tau]$ and $\|\boldsymbol{\sigma}\|$ generally occur at phase boundaries, as expected.

6.3.2 Comparison of stress distributions

Having observed that the occurrence of maximum values of $\lceil\tau\rceil$ and $\|\boldsymbol{\sigma}\|$ meets our expectations, we now proceed to compare the distributions of stresses on various porous grids to the distribution resulting from the regular grid. Firstly, for an in-depth comparison of the distribution of stresses in a porous grid as compared to a regular grid, one sample porous grid is selected. Accordingly, various metrics relating to these distributions are developed and applied to a wider set of porous grid. Finally, we hope to develop a relation between the porosity in a grid and the buildup of stresses in the respective grid. Throughout the analysis, the focus lays on the development of $\lceil\tau\rceil$. Only when peculiarities in the respective variable are observed, the work returns to $\|\boldsymbol{\sigma}\|$ to see if this variable exhibits similar behavior or behaves regularly.

In figures 23a and 23b, the development of $\lceil\tau\rceil$ as a result of the application of a sample phase-field on a regular and a sample porous grid is presented. Here, the elements are colored according to the maximum value of $\lceil\tau\rceil$ over the respective three edges incident on them. Firstly, $\lceil\tau\rceil$ appears to follow the contours of the imposed phase-field remarkably well, as we easily identify phase-interfaces from the distribution of Maximum values for $\lceil\tau\rceil$ occur at the interface between two phases, whereas in the bulk of a phase there are lower values for this jump in the shear stress. Secondly, comparing the regular to the porous grid, we observe that when an interface between phases coincides with a void, the associated buildup of $\lceil\tau\rceil$ is mitigated. A clear example of this occurs in the bottom right corner of the grid. Moreover, the buildup of $\lceil\tau\rceil$ at interfaces not covered by a void is reduced in some occasions, such as at the vertical interface in the top right corner. This indicates that the effect of porosity is not purely local.

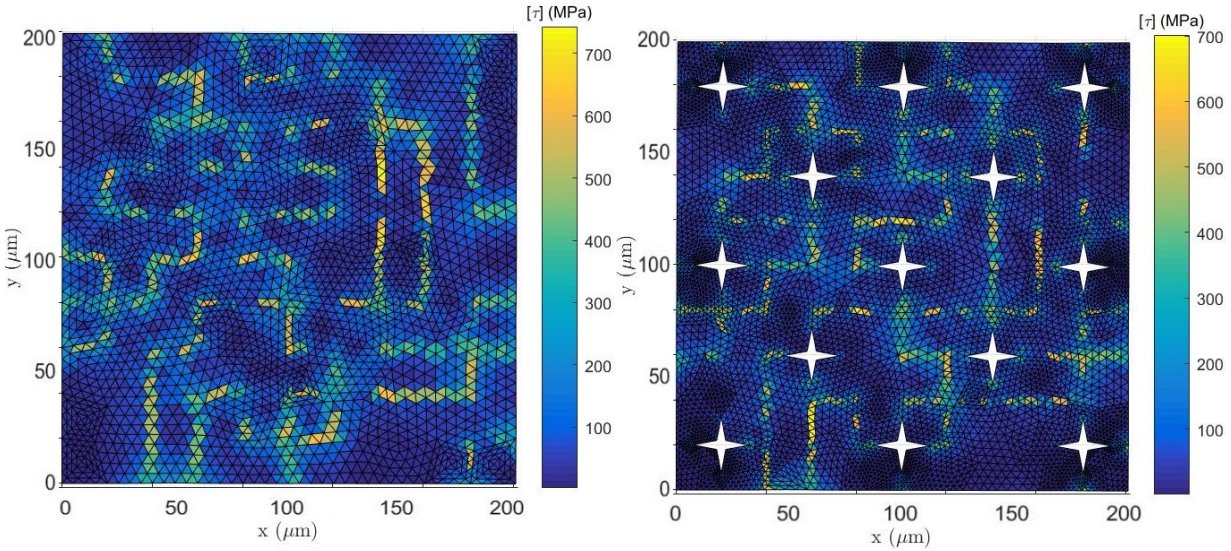

Figure 23: Elements in (a) a regular grid and (b) a porous grid colored according to the maximum value of $\lceil\tau\rceil$ over the three edges respectively incident on them, as a result of a sample phase-field.

Figure 24a presents the cumulative distribution function of $\lceil\tau\rceil$ over a simulated phase transition for the two grids, both with a dense mesh (as in figures 23a and 23b) and a sparse mesh, where the number of elements is lower by a factor 4. The values for $\lceil\tau\rceil$ of the edges are weighed

by the surface of the elements incident on the respective edge. This serves in order to account for the effect of the variation in element and edge size in the results.

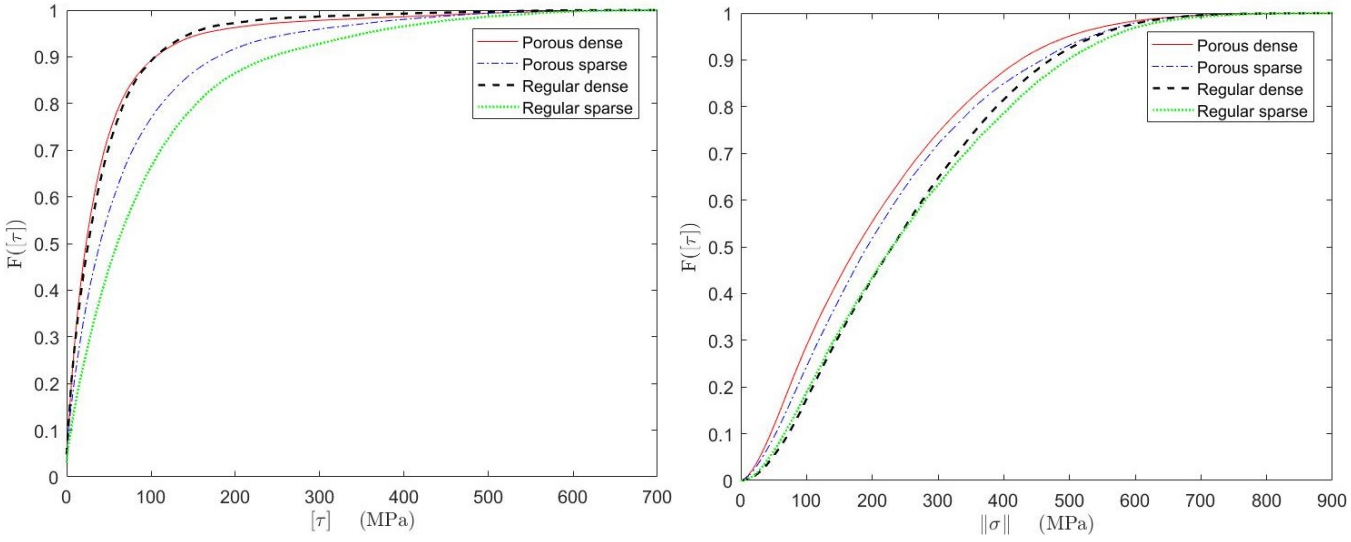

Figure 24: Cumulative distribution function of $\lceil \tau \rceil$ and $\|\boldsymbol{\sigma}\|$ for the two grids in a densely and sparsely meshed version. The effect of meshing seems to overrule any effect of the porosity on the distribution of $\lceil \tau \rceil$, whereas the distribution of $\|\boldsymbol{\sigma}\|$ is far less sensitive to the grid density.

The respective distributions, however, present us with a problem that is ought to be addressed before this work proceeds in discussing a bigger variety of porous grids. Namely, the effect of increasing the density of a mesh on the distribution of $\lceil \tau \rceil$ appears to overrule any effect due to the introduction of porosity into the grid.

The sensitivity of $\lceil \tau \rceil$ to the grid density follows from the following consideration. Firstly, the distribution of the components of $\boldsymbol{\sigma}$ and accordingly $\|\boldsymbol{\sigma}\|$ appears far less sensitive to the grid density, as can be seen in figure 24b. However, since $\lceil \tau \rceil$ registers the jump in the shear stress across an edge, this difference generally becomes smaller upon reduction of the element size. Accordingly, for both distributions of $\lceil \tau \rceil$ for the porous and regular grid, we observe a big shift towards lower values upon increasing the grid density. If the field of $\boldsymbol{\sigma}$ was continuous, this effect could be mitigated by weighing $\lceil \tau \rceil$ by for example the inverse of the size of the elements incident on the respective edges. Accordingly, we would derive a measure resembling the derivative of τ_{xy}. However, given the subdivision of the domain into grains and the discontinuity of the imposed phase-field, we expect discontinuities in τ_{xy} to persist upon infinitesimal grid refinement around grain boundaries. Accordingly, the proposed weighing by the inverse of the size of the incident elements would directly imply $\lceil \tau \rceil$ to explode towards infinity in this case. This proposes an essential difference in the required treatment of edges located in the bulk of a grain and those located at the interface between grains.

The values of $\lceil \tau \rceil$ at grain boundaries are exactly the values relevant to this study, as the development of discontinuities in shear stresses at grain boundaries is argued to lead to fracturing. Thus, by extracting the values of $\lceil \tau \rceil$ at the grain boundaries, we firstly highlight the physically most relevant metric and, secondly, are likely to largely mitigate the effect of the grid density

on the results. Accordingly, the distribution of $\lceil\tau\rceil$ at the boundaries between grains located in the bulk of the grid is considered in the remainder of this section. Here, also the edges incident on a void are included into the analysis, as the respective edges would have been positioned at a grain boundary in a regular, non-porous grid.

In figure 25, the cumulative distribution function for the values of $\lceil\tau\rceil$ is presented for a sparse and dense version of the grids as displayed in figures 23a and 23b. As desired, the distribution seems less sensitive to grid refinement than the complete functions as presented in 24a. For the denser grids, the distributions are slightly skewed to the left for low values of $\lceil\tau\rceil$, after which they pass under the respective function corresponding to the sparse grid for high values of $\lceil\tau\rceil$. The higher occurrence of low stresses results from what has been found above, namely that a grain boundary located between two grains in the same phase will have lower values for $\lceil\tau\rceil$ at a higher grid density. On the other hand, grid refinement on a boundary between two interfaces is likely to lead to higher values of $\lceil\tau\rceil$, since we found that $\|\boldsymbol{\sigma}\|$ does not converge at such locations. Accordingly, $\lceil\tau\rceil$, which derives from the components of $\boldsymbol{\sigma}$, is expected to increase upon grid refinement at such phase interfaces.

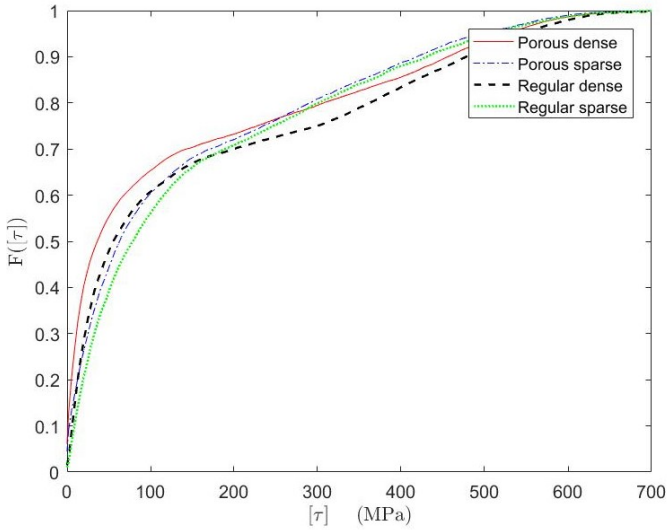

Figure 25: The distribution of $\lceil\tau\rceil$ at in-bulk grain boundaries on the grids in figures 23a and 23b (dense versions) and sparse versions. The influence of grid refinement on the grid refinement is reduced.

Moreover, from the regular to the porous grid, we do not observe a pronounced shift of the distribution towards lower values of $[\tau]$. Since the porous grid has a rather low porosity of 2.5% and contains voids only at a small fraction of the grain boundaries, it is of interest to consider if other degrees and positions of porosity do result in a pronounced shift of the distribution.

Taking the newly defined distribution $[\tau]$ across grain boundaries, we continue to evaluate different porous grids in terms of this distribution and see which factors, such as the number of voids and their dimensions, influence the distribution of $[\tau]$ in which manner. Let us define voids with various dimensions, as presented in figure 26. Grids A and B, respectively in figures 26a and 26b, have a porosity of 10%. Grid C in figure 26c has a porosity of 5% as it contains the voids from grid 26a scaled by a factor $\frac{1}{\sqrt{2}}$. Grid D in figure 26d has a porosity of about 5% by positioning the voids in figure 26a at every second location.

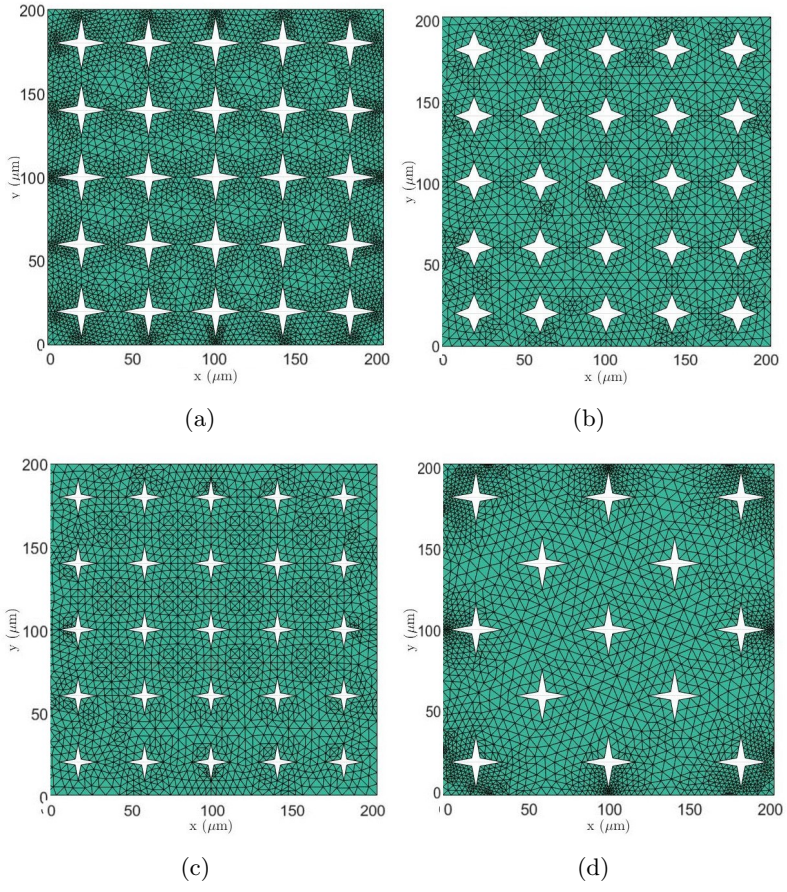

Figure 26: Grids subjected to phase transition, results of which are presented in figure 27.

The respective distribution functions over several simulated phase transitions are presented in figure 27. Firstly, it is evident that those grids with a high number of voids result in a shift of the distribution function of $\lceil \tau \rceil$ towards lower values. This suggests that the effect of the voids is local, in that it requires the direct presence of a void at a grain boundary to lead to a reduction in shear stresses. Among the three grids with a high number of voids, we see that the distribution for B and C are remarkably similar. Whereas the porosity in the former grid is 5% and to the latter is 10%, it seems that this similarity of the distributions is an expression of the fact that the voids have the same length along their longest dimension (the height of the triangles forming the star-shaped void). This suggests that what is actually the decisive factor in reduction of the values of $\lceil \tau \rceil$ at the grain boundaries is the fraction of these boundaries that is replaced by a void.

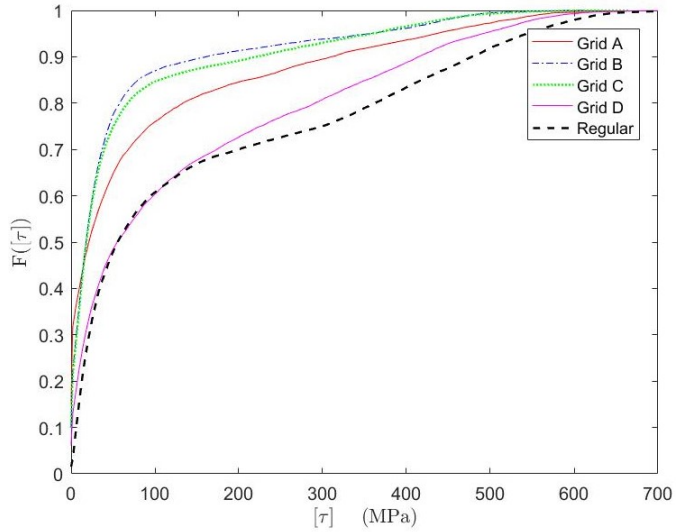

Figure 27: Cumulative distribution function of $\lceil \tau \rceil$ over grain boundaries resulting from repeated simulations of a phase transition on the grids in figures 26a to 26d.

However, along this same argument, we would expect grid A in figure26a to lead to the highest reduction of shearing stresses at grain boundaries, since here the voids have substituted for the biggest fraction of the grain boundaries. This does not follow from the given distribution function. To find a possible explanation for this observation, we now proceed with a closer analysis of the development of the distribution of $\lceil \tau \rceil$ as the voids in a grid are proportionally increase in size to establish a porosity from 2 to 10%, in steps of 2%. These voids are given the proportion equal to the voids in grid A and C.

The respective distribution functions are presented in figure 28a. Here, we see that all non-zero degrees of porosity lead to a shift of the distribution function of $\lceil \tau \rceil$ towards lower values. However, for the grids with 4 and 6% porosity, we observe that the distribution is skewed to the left, as compared to the distribution corresponding to higher degrees of porosity. The distributions of $\|\boldsymbol{\sigma}\|$, presented in 28b as a basic check on the model, do not violate our expectations. Here, higher degrees of porosity lead to lower levels of $\|\boldsymbol{\sigma}\|$.

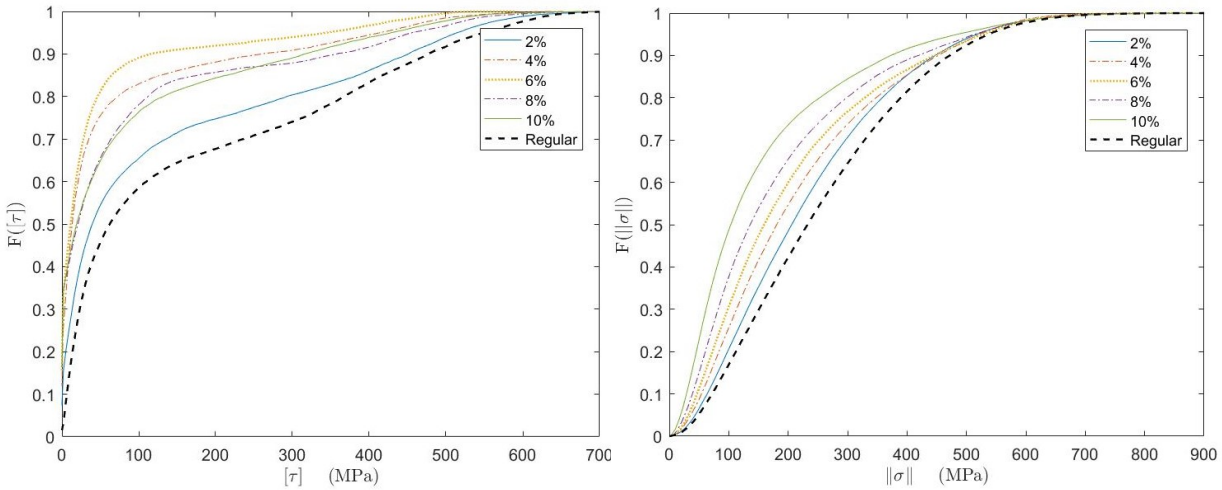

(a) (b)

Figure 28: Cumulative distribution function of $[\tau]$ over grain boundaries and $\|\boldsymbol{\sigma}\|$ over the whole grid, respectively presented in figures (a) and (b).

A consideration of the development of $[\tau]$ as a result of the same phase-field applied to the sample grids in figures 29a to 29d suggests why this shift of the distribution of $[\tau]$ occurs. Namely, the triangulation of the domain corresponding to 4 and 6% porosity has led to perfectly horizontal and vertical boundaries for a large part of the grains. Inspection of the fields of $[\tau]$ as compared to the other two grids suggests that when a phase interface occurs at such a vertical or horizontal boundary, the development of $[\tau]$ is largely mitigated. This leads us to the conclusion that the orientation of grain boundaries influences the development of $[\tau]$, even more so than the degree of porosity.

This is definitely an interesting and valuable result. However, if we seek to find a relation between the degree of porosity and the development of $[\tau]$ over grain boundaries, the results need to be isolated from this effect induced by the orientation of edges composing the grain boundaries. In order to do so, the following approach has been followed. Namely, the function provided by the PDE Toolbox to mesh a domain in steps is used. Firstly, for each porous grid, the triangulated porous domain is taken as a starting point. Subsequently, the voids are triangulated in order to establish a fully triangulated domain. As a result, the porous grid and the associated regular grid generally coincide on the nonporous parts of the domain, reducing the effect of the orientation of edges at the boundaries between grains. The match on the nonporous parts of the domain is not perfect, however, since slight adjustment of the grid occur here as well.

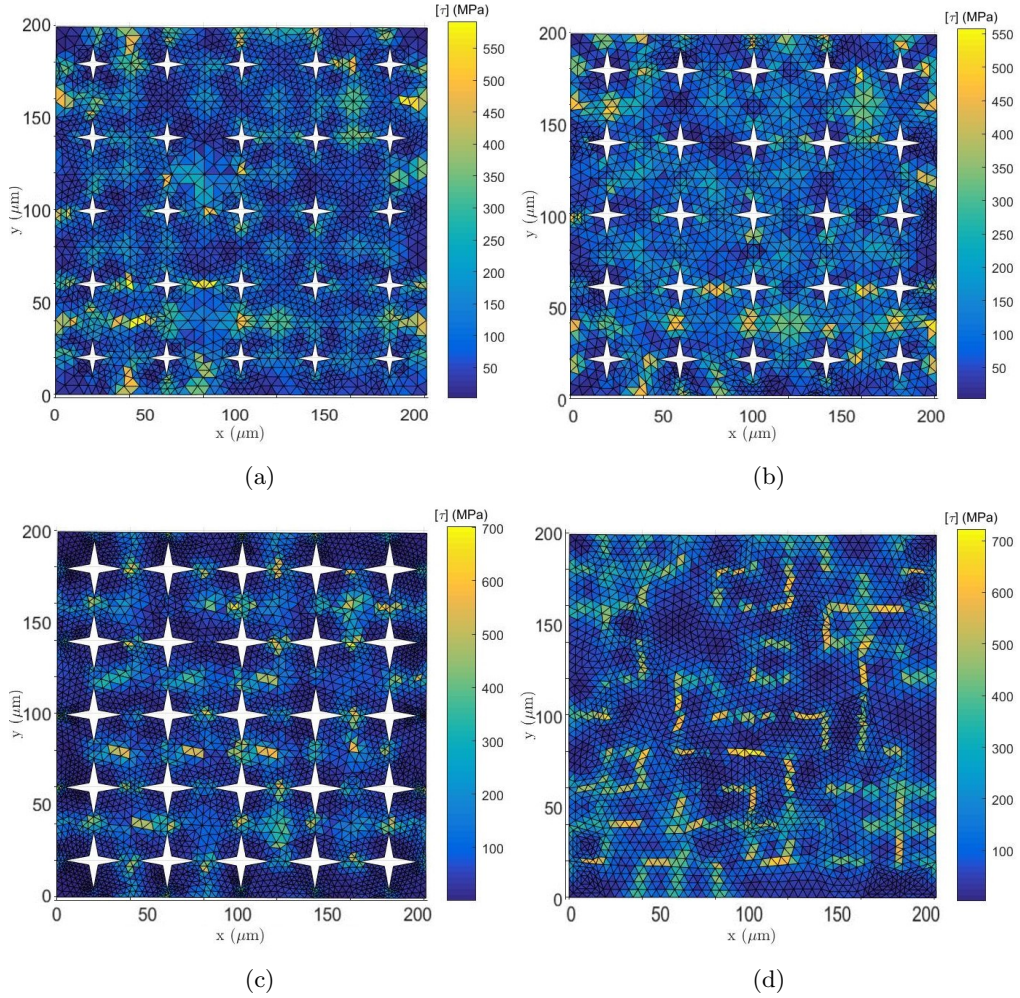

Figure 29: Sample distributions of $[\tau]$ resulting from the same phase-field applied to grids with porosities of 4%, 6%, and 10% and a regular grid, respectively in (c), (d), (e), and (f).

Figures 30a to 30c present the grain boundaries for a 3% porous grid, the regular grid meshed according to the above procedure and a regular grid due to the direct triangulation of the domain. It is evident that, although not perfect, the coincidence of the grain boundaries between the former two grids is greater than that between the porous grid and the grid due to direct triangulation. The shift in the distribution of $[\tau]$ across grain boundaries for the non-porous grid corresponds to what one would expect based on the above analysis, namely that a higher coincidence of the orientation of edges at the grain boundaries leads to the distribution functions of the respective grids laying closer to each other.

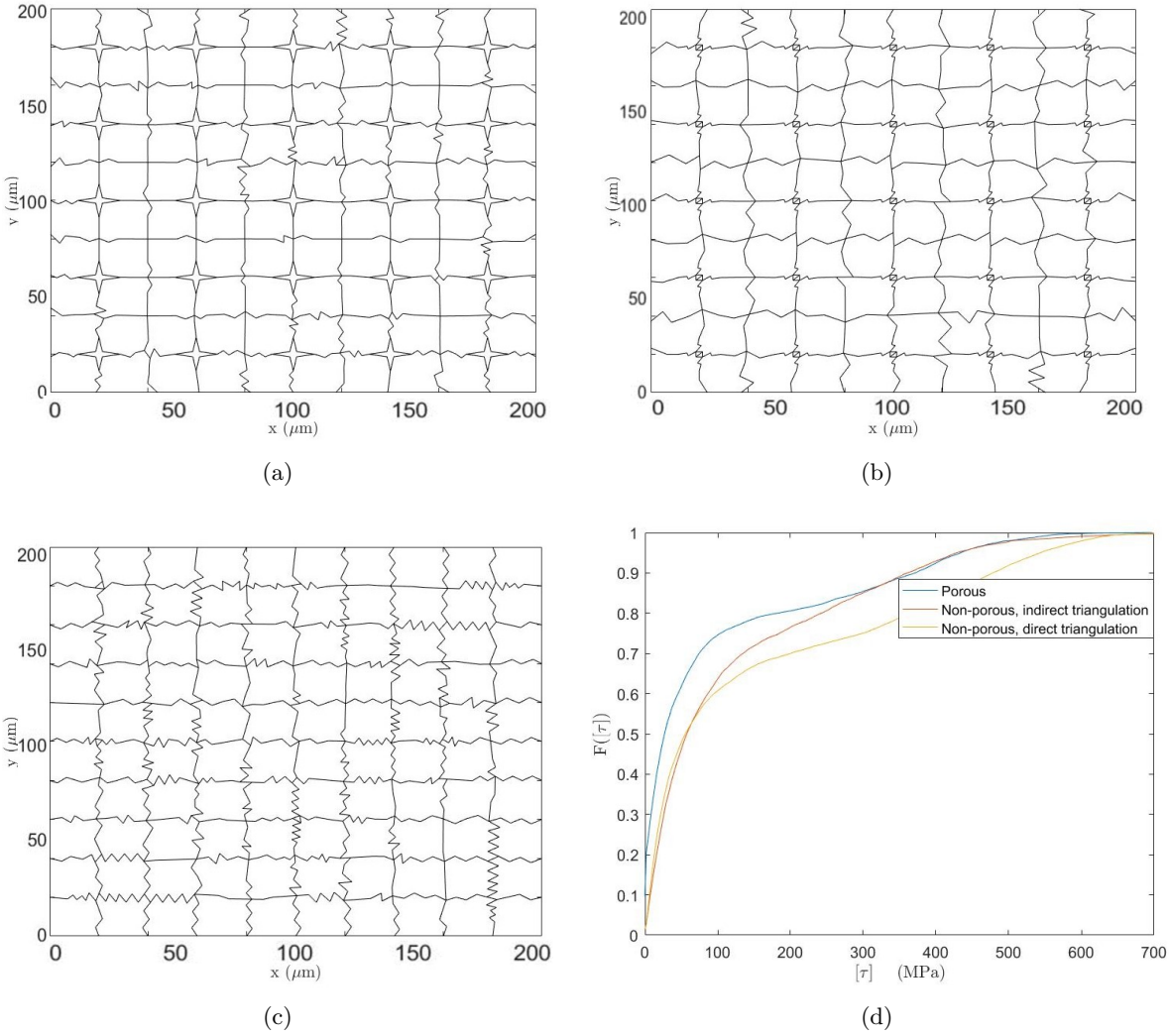

Figure 30: Example of the grain boundaries resulting from the indirect triangulation of a full grid as discussed in the text. Grain boundaries corresponding to (a) Porous grid (3%) (b) Indirectly triangulated full grid (c) Directly triangulated full grid. The cumulative distribution function of $\lceil \tau \rceil$ shows that the change in triangulation skews thee distribution of $\lceil \tau \rceil$ at grain boundaries towards lower values.

For each degree of porosity, the procedure as outlined above has been followed. Subsequently, the distributions of $\lceil \tau \rceil$ across grain boundaries for the porous grid can be compared to the distribution corresponding to the indirectly triangulated grid. Since we would like to analyse the trend in $\lceil \tau \rceil$ in terms of the degree of porosity, we consider the following parameters. Namely, for each degree of porosity, the value of $\lceil \tau \rceil$ corresponding to a set of percentiles (50, 80, 90, 95, 99, and 99.5%) in the cumulative distribution functions is extracted. The relative difference of the respective values with respect to the value corresponding to the same percentile in the full grid is subsequently computed. An example, corresponding to the 80^{th} percentile, is plotted in figure 31a. Here, it is evident that, although increasing, the positive effect of the degree of porosity on the decrease in the values of $\lceil \tau \rceil$ is far from monotonous. This stems mostly from the still limited control over the orientation of the edges at grain boundaries we possess.

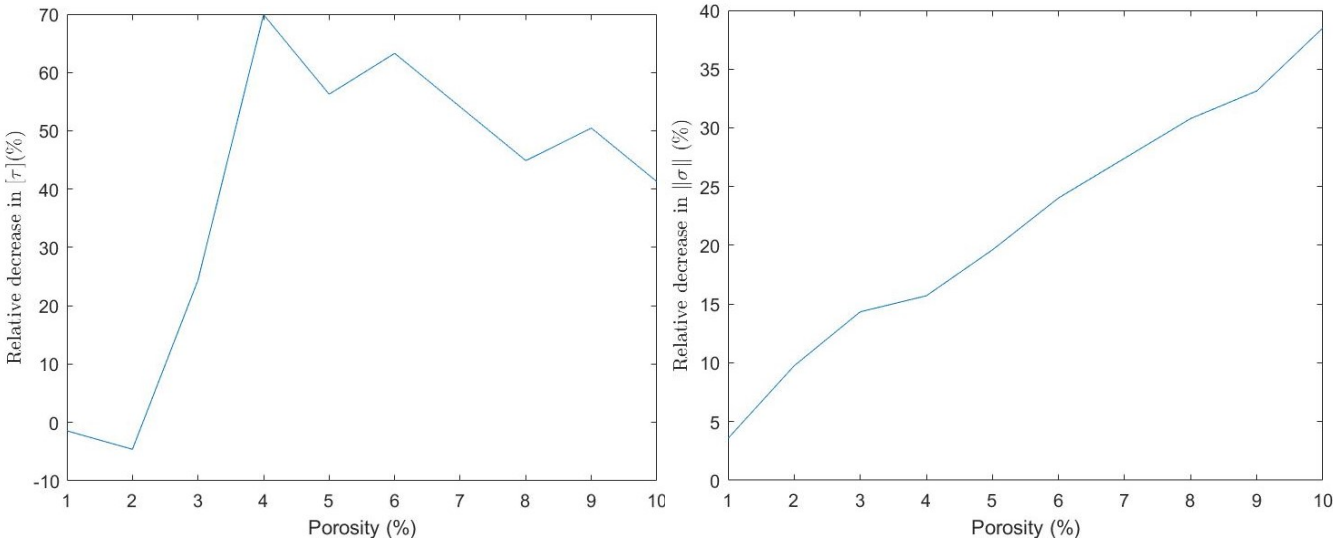

(a) (b)

Figure 31: Relative decrease in the values of (a) $\lceil\tau\rceil$ and (b) $\|\boldsymbol{\sigma}\|$ corresponding to the 80$^{\text{th}}$ percentile plotted against porosity.

The respective values were linearly regressed on the degree of porosity. The results are presented in the left part of table 10. It appears that the shift in the values for $\lceil\tau\rceil$ corresponding to the lower percentiles is greatest. This is not surprising, since here the relative share of free grain boundaries at voids is greatest. The effect reduces as we consider higher percentiles. Since in the present implementation, there are grain boundaries that are not incident on a void as well, the occurrence of extremes at the respective locations is relatively untouched. This corresponds to the observation that the effect of voids on the distribution of $\lceil\tau\rceil$ is rather local.

Table 10: Coefficients of the relative decrease in $\lceil\tau\rceil$ corresponding to the k$^{\text{th}}$ percentile, y, regressed on porosity, x: $y = \alpha \cdot x + \beta$ (left), and on the part of in-bulk grain boundaries incident on a void, x': $y = \gamma \cdot x' + \delta$ (right).

Percentile	α	β (%)	R^2		γ	δ (%)	R^2
50	6 ± 2	1 ± 1	0.54		2.3 ± 0.7	-7 ± 20	0.68
80	5 ± 3	11 ± 18	0.33		1.9 ± 0.9	-15 ± 28	0.44
90	2 ± 3	2 ± 17	0.10		0.8 ± 0.9	-10 ± 27	0.14
95	1.1 ± 0.6	-2 ± 3	0.38		0.4 ± 0.2	-6 ± 6	0.35
98	1.3 ± 0.8	2 ± 5	0.34		0.5 ± 0.2	-4 ± 8	0.39
99	1.5 ± 0.9	4 ± 6	0.34		0.6 ± 0.3	-4 ± 9	0.42
99.5	2 ± 1	7 ± 7	0.27		0.6 ± 0.4	-1 ± 11	0.35

Moreover, in the closer analysis of the behavior of $\lceil\tau\rceil$ across grain boundaries on the grids in figure 26, it appeared that the distribution of the respective variable was not so much dependent on the percentages of the domain filled with voids as on the parts of the grain boundaries substituted by a void. Accordingly, the relative decreases in $\lceil\tau\rceil$ of the k$^{\text{th}}$ percentile were linearly regressed on the percentage of grain boundaries that were replaced by a void. Here, the

structure with 10% porosity has 40% of its bulk grain boundaries replaced by a void. Thus, a structure with a porosity of $\frac{10\%}{n}$ has $\frac{40\%}{\sqrt{n}}$ of its grain boundaries replaced by a void.

The resulting regression coefficients are presented in the right part of table 10. The higher values of R^2 resulting from the linear regression of the relative decrease in $\lceil\tau\rceil$ on this variable support the argument that the respective variable is more important in relating porosity to the development of $\lceil\tau\rceil$ than the degrees of porosity.

The same analysis was performed on the decrease in $\|\boldsymbol{\sigma}\|$ corresponding to the same selection of percentiles. The results are presented in table 11. Here, two observations can be made. Firstly, as compared to the results of $\lceil\tau\rceil$, the decreases in $\|\boldsymbol{\sigma}\|$ have a better fit, as expressed in the higher values for R^2. This confirms the observation that decreases in $\|\boldsymbol{\sigma}\|$ were far more consistent in the increases in porosity. For the lower percentiles, the decreases in $\|\boldsymbol{\sigma}\|$ have a close to perfect linear fit. Moreover, here as well the percentage of in-bulk grain boundaries is a better predictor of the decrease in $\|\boldsymbol{\sigma}\|$ than the percentage of porosity.

Table 11: Coefficients of the relative decrease in $\|\boldsymbol{\sigma}\|$ corresponding to the k^{th} percentile regressed on porosity, x: $y = \alpha \cdot x + \beta$ (left), and on the part of in-bulk grain boundaries incident on a void, x': $y = \gamma \cdot x' + \delta$ (right).

Percentile	α	β (%)	R^2		γ	δ (%)	R^2
50	5.3 ± 0.2	1 ± 1	0.99		1.8 ± 0.2	-21 ± 3	0.98
80	3.6 ± 0.2	2 ± 1	0.99		1.23 ± 0.08	-13 ± 2	0.98
90	2.2 ± 0.2	2 ± 1	0.95		0.73 ± 0.08	-7 ± 2	0.93
95	1.1 ± 0.2	3 ± 1	0.88		0.38 ± 0.05	-2 ± 2	0.91
98	0.5 ± 0.2	3 ± 1	0.54		0.20 ± 0.06	0 ± 2	0.66
99	0.5 ± 0.3	2 ± 1	0.35		0.2 ± 0.1	0 ± 2	0.46
99.5	0.6 ± 0.4	2 ± 2	0.30		0.2 ± 0.1	-2 ± 4	0.39

6.4 Discussion

In this part of the present thesis, a 2D model has been proposed to simulate the development of stresses due to the structural transition associated with a first order magnetic phase transition. The application of this model to two grids with different implementations of porosity has provided plenty of insights, both into the workings of the FEM in relation to the general problem as into the influence of porosity on the development of shear stresses in a material. These insights will be elaborated in this section.

Firstly, the relation between the orientation of an edge and the value of the discontinuity in the shear stress $\left[\tau\right]$ over this edge is physically relevant, but it also influences the results regarding the respective variable in a way that is hard to fully account for. It is physically relevant in the sense that the given relation indicates that, with the eye on reducing the buildup of shearing stresses in a material, some edge orientations are preferred over others. In the present model, these directions appeared to be coincident with the x- and y-axis. The relation between the orientation of an edge and the buildup of shear stresses, which is evident from equation 49, is subject to physical experiments. For example, experiments in [47] find that crack formation in crystals often occurs in planes inclined to the axis along which forces are loaded onto a body. In our model, these loading axes were the x- and y-axes, whereas no shearing deformation was imposed. Accordingly, it could have been expected that $\left[\tau\right]$ would be damped for horizontally or vertically oriented edges.

The influence on the distribution of $\left[\tau\right]$ of the orientation of edges has been evident and attempts have been made in the present work to reduce this impact through indirect meshing of the regular domain. However, in order to fully account for this effect, one would have to apply meshing algorithms that depart from the delaunay triangulation algorithm and are more delicate than the meshing applied in grid type 1. On the other hand, the same relation between grain boundary orientation and shearing stresses forms an interesting venue of further study, possibly with the eye on designing systems with reduced buildups of $\left[\tau\right]$ across grain boundaries.

In terms of the physical predictions of the model, it has appeared difficult to extract a meaningful quantitative measure for the influence of porosity on the shearing stresses in a material. The linear regression coefficient in tables 10 and 11 do confirm the expected effect of porosity in reducing stresses by the substitutions of voids for grain boundaries. However, since this is a 2D-model with a rather artificially implemented system of grains and voids, it would be difficult to extrapolate the results to our physical world. The qualitative insights provided by this model are arguably more interesting.

The part of grain boundaries incident on a void has appeared to have a higher explanatory power in the reduction of $\left[\tau\right]$ across grain boundaries than the percentage of porosity in in a grid. This is not so surprising, if we consider the following. Namely, in a hypothetical situation where for each grain, the full boundary would be incident on a void, rendering us with floating grains, all grains should be able to assume their equilibrium dimensions at all times. This, of course, is under the assumption that the respective voids are wide enough to allow for transformations without neighboring grains getting into touch. This is a sufficient provision to establish a body without stresses. It follows logically that the fraction of grain boundaries incident on a void, and not the degree of porosity, predicts the accumulation of $\left[\tau\right]$ across grain boundaries best.

7 Conclusion

The central topic in the present thesis has been magnetic phase transitions. To gain insights into these transitions, two modelling endeavours have been discussed.

Firstly, DFT as implemented in VASP-software has been applied to model the lithiation of the ferromagnetic material Fe_2P and to find a proxy for the development of the transition temperature of this material upon lithiation. The results suggest that clustering of Li-atoms occurs in the a, b-plane at $3g$-positions formerly occupied by Fe-atoms. Given the fact that these are the positions in the mixed-magnetic Fe_2P at which the Fe-atoms carry a high magnetic moment, this substitution of non-magnetic Li-atoms for magnetic Fe-atoms seems to lead to a considerable reduction of the total magnetic moment per formula unit.

Furthermore, attempts have been discussed to proxy a paramagnetic state for the lithiated structure. It was found that this artificial structure with every second $3g$-layer lithiated has a ground state in which alternating layers along the c-axis have opposite magnetic moments. Moreover, the energy difference between $Fe_{1.5}Li_{0.5}P$ in a ferromagnetic state and the material with a paramagnetic ordering in the a, b-plane decreases linearly in the number of $3g$-positions containing iron. Accordingly, we would expect the T_C of this structure to decrease upon lithiation as well, which contradicts experimental findings in [9]. This discrepancy between the results as presented here and the experimental findings could stem from the fact that in this work higher lithiation fractions were used than those achieved experimentally, or from an improperly selected proxy for the paramagnetic state.

Secondly, an FEM-model has been developed to model the structural changes in a 2D material during a first order magnetic phase transition. Here, the static equilibrium in the displacement field for a domain of grains due to the imposition of a phase-field was approximated. The first grid to be implemented, high in symmetry but correspondingly highly artificial, did not exhibit the expected occurrence of maximum values in the discontinuity of shear stresses, $\llbracket \tau \rrbracket$, at interfaces between the two faces. Accordingly, it was rejected. A second grid did show this expected results, and was therefore taken into closer analysis of the development of stresses during a phase transition.

Hereafter, voids were introduced into the domain, along grain boundaries, to model the presence of porosity in a material. The distribution of $\|\boldsymbol{\sigma}\|$ skewed towards lower values upon the expansion of voids in the domain. The distribution of $\llbracket \tau \rrbracket$, however, appeared more sensitive to other modelling decisions. After the focus was laid on the values of $\llbracket \tau \rrbracket$ across grain boundaries, it was found that the distributions of this variable was highly sensitive to the orientation of the edges composing these grain boundaries. After a correction for this effect, a positive relation was identified between the degree of porosity and the relative reduction in $\llbracket \tau \rrbracket$ across grain boundaries. However, the part of grain boundaries incident on a void appeared to be a better predictor of the reduction in $\llbracket \tau \rrbracket$, which corresponds to experimental findings. More delicate development of the grid to correspond to physically realistic orientations of grain boundaries is needed to gain more robust quantitative measures for this relation. Moreover, the relation between the orientation of grain boundaries and shearing stresses at these boundaries forms an interesting venue for further research to which the present FEM-model can be readily applied.

References

[1] Tishin, A. M., Spichkin, Y. I. (2016). *The magnetocaloric effect and its applications.* CRC Press.

[2] Smith, A. (2013). Who discovered the magnetocaloric effect?. European Physical Journal H, 38, 507-517.

[3] Pecharsky, V. K., Gschneidner Jr, K. A. (1999). Magnetocaloric effect and magnetic refrigeration. *Journal of Magnetism and Magnetic Materials, 200*, 44-56.

[4] Gschneidner Jr, K. A., Pecharsky, V. K., Tsokol, A. O. (2005). Recent developments in magnetocaloric materials. *Reports on progress in physics, 68*, 1479-1539.

[5] Tesla, N. (1889). *U.S. Patent No. 396,121.* Washington, DC: U.S. Patent and Trademark Office.

[6] Boeije, M. F. J., Roy, P., Guillou, F., Yibole, H., Miao, X. F., Caron, L., Banerjee, D., Van Dijk, N., De Groot, R., Bruck, E. (2016). Efficient room-temperature cooling with magnets. *Chemistry of Materials, 28*, 4901-4905.

[7] Hudl, M., Campanini, D., Caron, L., Höglin, V., Sahlberg, M., Nordblad, P., Rydh, A. (2014). Thermodynamics around the first-order ferromagnetic phase transition of Fe_2P single crystals. *Physical Review B, 90*, 144432(1)-144432(5).

[8] Caron, L., Hudl, M., Höglin, V., Dung, N. H., Gomez, C. P., Sahlberg, M., Brück, E., Andersson, Y. Nordblad, P. (2013). Magnetocrystalline anisotropy and the magnetocaloric effect in Fe_2P. *Physical Review B, 88*, 094440.

[9] Lindeborg, K. G. (2017) First Lithiation of the Fe_2P-based Magnetocaloric Materials (Master's Thesis) Delft University of Technology, Delft.

[10] Gschneidner Jr, K. A., Pecharsky, V. K. (2000). Magnetocaloric materials. *Annual Review of Materials Science, 30*, 387-429.

[11] Liu, J., Gottschall, T., Skokov, K. P., Moore, J. D., Gutfleisch, O. (2012). Giant magnetocaloric effect driven by structural transitions. *Nature materials, 11*, 620-626.

[12] Brown, G. V. (1976). Magnetic heat pumping near room temperature. *Journal of Applied Physics, 47*, 3673-3680.

[13] Pecharsky, V. K., Gschneidner Jr, K. A. (1997). Giant magnetocaloric effect in $Gd_5(Si_2Ge_2)$. *Physical review letters, 78*, L179-L184.

[14] Şaşioglu, E., Sandratskii, L. M., Bruno, P. (2005). First-principles study of exchange interactions and Curie temperatures of half-metallic ferrimagnetic full Heusler alloys $Mn_2VZ(Z = Al, Ge)$. of Physics: Condensed Matter, 17, 995.

[15] Gutfleisch, O., Willard, M. A., Brück, E., Chen, C. H., Sankar, S. G., Liu, J. P. (2011). Magnetic materials and devices for the 21^{st} century: stronger, lighter, and more energy efficient. *Advanced materials, 23*, 821-842.

[16] Lundgren, L., Tarmohamed, G., Beckman, O., Carlsson, B., Rundqvist, S. (1978). First order magnetic phase transition in Fe_2P. *Physica Scripta, 17*, 39-50.

[17] Belyea, D. D., Lucas, M. S., Michel, E., Horwath, J., Miller, C. W. (2015). Tunable magnetocaloric effect in transition metal alloys. *Scientific reports*, 5, 15755-15762.

[18] Waske, A., Giebeler, L., Weise, B., Funk, A., Hinterstein, M., Herklotz, M., Skokov, K., Fahler, S., Gutfleisch, O., Eckert, J. (2015). Asymmetric first-order transition and interlocked particle state in magnetocaloric $La(Fe, Si)_{13}$. *Physica status solidi (RRL)–Rapid Research Letters, 9*, 136-140.

[19] Miao, X. F., Caron, L., Gercsi, Z., Daoud-Aladine, A., Van Dijk, N. H., Brück, E. (2015). Thermal-history dependent magnetoelastic transition in $(Mn, Fe)_2(P, Si)$. *Applied Physics Letters, 107*, 1-5.

[20] Lyubina, J., Schäfer, R., Martin, N., Schultz, L., Gutfleisch, O. (2010). Novel design of $La(Fe, Si)_{13}$ alloys towards high magnetic refrigeration performance. *Advanced Materials, 22*, 3735-3739.

[21] M. I. Aroyo, A. Kirov, C. Capillas, J. M. Perez-Mato H. Wondratschek. (2006) Bilbao Crystallographic Server II: Representations of crystallographic point groups and space groups. *Acta Cryst A62*, 115-128.

[22] Villars, P., Calvert, L. D., Pearson, W. B. (1985). Pearson's Handbook of Crystallographic Data for Intermetallic Phases. Volumes 1, 2, 3. *American Society for Metals, 1985*, 3258.

[23] Tobola, J., Bacmann, M., Fruchart, D., Kaprzyk, S., Koumina, A., Niziol, S., Zach, R. (1996). Magnetism of Fe_2P investigated by neutron experiments and band structure calculations. *Journal of magnetism and magnetic materials, 157*, 708-710.

[24] Dung, N. H., Ou, Z. Q., Caron, L., Zhang, L., Thanh, D. T. C., De Wijs, G. A., De Groot, R., Buschow, K., Brück, E. (2011). Mixed magnetism for refrigeration and energy conversion. *Advanced Energy Materials, 1*, 1215-1219.

[25] Liu, X. B., Liu, J. P., Zhang, Q., Altounian, Z. (2013). Fe magnetic moment formation and exchange interaction in Fe_2P: A first-principles study. *Physics Letters A, 377*, 731-735.

[26] Hasnip, P. J., Refson, K., Probert, M. I., Yates, J. R., Clark, S. J., Pickard, C. J. (2014). Density functional theory in the solid state. *Philosophical Transactions of the Royal Society A: Mathematical, Physical and Engineering Sciences, 372*, 1-26.

[27] Kohn, W., Becke, A. D., Parr, R. G. (1996). Density functional theory of electronic structure. *The Journal of Physical Chemistry, 100*, 12974-12980.

[28] Kresse, G., Marsman, M. Furthmuller, J. (2018) *VASP the Guide*, University of Vienna.

[29] Ahmed, M. A., Okasha, N., Oaf, M., Kershi, R. M. (2007). The role of Mg substitution on the microstructure and magnetic properties of Ba Co Zn W-type hexagonal ferrites. *Journal of magnetism and magnetic materials, 314*, 128-134.

[30] Roy, P., Torun, E., de Groot, R. A. (2016). Effect of doping and elastic properties in $(Mn, Fe)_2(Si, P)$. *Physical Review B, 93*, 094110.

[31] Clementi, E., Raimondi, D. L., Reinhardt, W. P. (1967). Atomic screening constants from SCF functions. II. Atoms with 37 to 86 electrons. *The Journal of Chemical Physics, 47*, 1300-1307.

[32] Ong, S. P., Wang, L., Kang, B., Ceder, G. (2008). $LiFePO_2$ phase diagram from first principles calculations. of Materials, 20, 1798-1807.

[33] Boyanov, S., Bernardi, J., Gillot, F., Dupont, L., Womes, M., Tarascon, J. M., Doublet, M. L. (2006). FeP: another attractive anode for the Li-ion battery enlisting a reversible two-step insertion/conversion process.*Chemistry of materials, 18*, 3531-3538.

[34] Zienkiewicz, O. C., Taylor, R. L., Zienkiewicz, O. C., Taylor, R. L. (1977). *The finite element method* (Vol. 36). London: McGraw-hill.

[35] Van Kan, J., Segal, A., Vermolen, F. (2008). *Numerical Methods in Scientific Computing*. Department of Applied Mathematics. Delft University of Technology, The Netherlands.

[36] Chadwick, P. (2012). *Continuum mechanics: concise theory and problems*. New York, Courier Corporation.

[37] Nikishkov, G.P. (2004) *Introduction to the finite element method [Lecture Notes]* Retrieved from nliebeaux.free.fr

[38] Schapery, R. A. (1968). Thermal expansion coefficients of composite materials based on energy principles. *Journal of Composite Materials, 2*, 380-404.

[39] Rice, J. (1985). *Is the aspect ratio significant for finite element problems? No. 85-535* Department of Computer Science, Purdue University

[40] MathWorks (2019) *Partial Differential Equation Toolbox User's Guide*. Retrieved from www.mathworks.com

[41] Lee, D. T., Schachter, B. J. (1980). Two algorithms for constructing a Delaunay triangulation. *International Journal of Computer Information Sciences, 9*, 219-242.

[42] Meyer, C. D. (2000).*Matrix analysis and applied linear algebra (Vol. 71)*. Philedelphia: SIAM.

[43] Cosgrove, J. W., Hudson, J. A. (2016).*Structural Geology and Rock Engineering*. World Scientific Publishing Company.

[44] Roylance, D. (2001). Transformation of stresses and strains. *Lecture Notes for Mechanics of Materials*. MIT, Cambridge

[45] Gramoll, K. (2019) *Multimedia Engineering Mechanics of Materials*. Accessible through www.ecourses.ou.edu

[46] Ostoja-Starzewski, M. (2007). *Microstructural randomness and scaling in mechanics of materials*. London, Chapman and Hall/CRC.

[47] Chen, Q., Liu, H. W. (1988). Resolved shear stress intensity coefficient and fatigue crack growth in large crystals. *Theoretical and applied fracture mechanics, 10*, 111-122.

A Appendix to part I

Throughout the VASP calculations presented in this thesis, different sampling parameters and convergence criteria have been applied, dependent on the respective structure and the accuracy required for the interpretation of the respective results. For converged calculations, values for σ an κ were used corresponding to a convergence of the total energy within the boundary of 1 meV with respect to the respective parameters. These parameters and criteria are presented in the table below.

Table 12: Sampling and convergence parameters applied to VASP calculations in the indicated figures and tables.

Result/ Structure	EDIFF (eV)	ENCUT (eV)	Degrees of Freedom	σ	k-grid
Figure 3	10^{-3}	650	Positions	0.1	$2 \times 2 \times 2$
Figures 4, 6a, 6b, 8, 13					
Tables 2, 3, 4	10^{-5}	650	Positions and lattice	0.05	$7 \times 7 \times 10$
Li bcc	10^{-5}	650	Positions and lattice	0.05	$24 \times 24 \times 24$
Fe bcc	10^{-5}	450	Positions and lattice	0.05	$22 \times 22 \times 22$
Figure 5	10^{-5}	650	Positions	0.1	$2 \times 2 \times 2$
Figure 10	10^{-3}	650	Positions	0.1	$7 \times 7 \times 5$